PHYSICAL REVIEW B **79**, 205434 (2009)

Resonant coherent phonon spectroscopy of single-walled carbon nanotubes

G. D. Sanders,[1] C. J. Stanton,[1] J.-H. Kim,[2] K.-J. Yee,[2] Y.-S. Lim,[3] E. H. Hároz,[4] L. G. Booshehri,[4] J. Kono,[4] and R. Saito[5]
[1]*Department of Physics, University of Florida, Box 118440, Gainesville, Florida 32611-8440, USA*
[2]*Department of Physics, Chungnam National University, Daejeon 305-764, Republic of Korea*
[3]*Department of Applied Physics, Konkuk University, Chungju, Chungbuk 380-701, Republic of Korea*
[4]*Department of Electrical and Computer Engineering, Rice University, Houston, Texas 77005, USA*
[5]*Department of Physics, Tohoku University, Sendai 980-8578, Japan*

(Received 10 December 2008; revised manuscript received 26 March 2009; published 29 May 2009)

Using femtosecond pump-probe spectroscopy with pulse-shaping techniques, one can generate and detect coherent phonons in chirality-specific semiconducting single-walled carbon nanotubes. The signals are resonantly enhanced when the pump photon energy coincides with an interband exciton resonance, and the analysis of such data provides a wealth of information on the chirality dependence of light absorption, phonon generation, and phonon-induced band-structure modulations. To explain our experimental results, we have developed a microscopic theory for the generation and detection of coherent phonons in single-walled carbon nanotubes using a tight-binding model for the electronic states and a valence force field model for the phonons. We find that the coherent phonon amplitudes satisfy a driven oscillator equation with the driving term depending on photoexcited carrier density. We compared our theoretical results with experimental results on mod 2 nanotubes and found that our model provides satisfactory overall trends in the relative strengths of the coherent phonon signal both within and between different mod 2 families. We also find that the coherent phonon intensities are considerably weaker in mod 1 nanotubes in comparison with mod 2 nanotubes, which is also in excellent agreement with experiment.

DOI: 10.1103/PhysRevB.79.205434 PACS number(s): 78.67.Ch, 73.22.−f

I. INTRODUCTION

Single-walled carbon nanotubes (SWNTs) can be viewed as rolled-up sheets of graphene, having a one-dimensional band structure with unique electronic, mechanical, and optical properties. Their electronic properties vary significantly, depending on their chirality indices (n,m) and can be either metallic or semiconducting.[1–5] Although there are currently worldwide efforts to achieve single-chirality samples, a standard for fabrication of such samples has yet to be established. Resonant Raman spectroscopy (RRS) or photoluminescence excitation (PLE) spectroscopy is usually used to study chirality-dependent electronic and vibrational properties. However, carbon nanotube samples typically contain ensembles of nanotubes with different chiralities and the unknown relative abundances of different-chirality tubes in such samples often makes it challenging to extract reliable parameters on chirality-dependent properties from experimental results.

Resonant Raman spectroscopy can be used to study chirality-dependent electron-phonon coupling in nanotubes and can be used to uniquely determine the chirality of individual tubes.[6–10] Raman spectroscopy is a sensitive probe of ground-state vibrations but is less suitable for studying excited-state vibrational properties. Recently, excited-state lattice vibrations in carbon nanotubes have been studied with coherent phonon (CP) spectroscopy.[11–14] In CP spectroscopy, coherent phonon oscillations are excited by pumping with an ultrafast pump pulse and are detected by measuring changes in the differential transmission using a delayed probe pulse. The CP intensity is then obtained by taking the temporal power spectrum of the differential transmission. The peaks in the power spectrum correspond to coherent phonon frequencies. Coherent phonon spectroscopy allows direct measurement of excited-state phonon dynamics in the time domain including phase information and dephasing times.

We have developed a technique that allows us to study chirality-dependent properties of nanotubes in an ensemble.[15] This is described in Sec. II. By shaping the pump pulse, we incorporate quantum control techniques in CP spectroscopy. Using predesigned trains of femtosecond optical pulses, we have selectively excited and probed coherent lattice vibrations of the radial breathing mode (RBM) of specific chirality single-walled carbon nanotubes. We are able to gain information on light absorption, coherent phonon generation, and coherent phonon-induced band-structure modulations. We find that coherent RBM phonons can be selectively excited by using a train of pump pulses whose repetition rate is in resonance with the desired phonon frequency. By exciting only those phonon modes with a specific frequency, we can selectively study nanotubes with the same chirality in an ensemble of tubes.

In order to explain our experimental results, we develop in Sec. III a microscopic theory for the generation and detection of coherent phonon lattice vibrations in carbon nanotubes by ultrafast laser pulses. We use a third nearest-neighbor extended tight-binding (ETB) model to describe the electronic states over the entire Brillouin zone while the phonons are treated in a valence force field model. In treating the electrons and phonons, we exploit the screw symmetry of the nanotube to drastically simplify the problem. Equations of motion for each CP vibrational mode are obtained using a microscopic description of the electron-phonon interaction based on direct evaluation of the three-center electron-phonon matrix elements using *ab initio* wave functions and screened atomic potentials. For each CP active mode we find that the CP amplitudes satisfy a driven oscillator equation with a coherent phonon driving function that depends on photoexcited hot carrier distributions. An ultrafast laser pulse generates electron-hole pairs and the driving function rises sharply in a steplike fashion. If the pulse duration is shorter than the phonon oscillation period, the rapid initial jump in the coherent phonon driving function gives rise to oscillating coherent phonon amplitudes.

Carbon nanotubes with the same values of $2n+m$ are said to belong to the same family (with index $2n+m$). Carbon nanotubes in a given family are metallic if $\mathrm{mod}(n-m,3)=0$ and semiconducting otherwise. The semiconducting tubes are classified as either mod 1 or mod 2 depending on whether the value of $\mathrm{mod}(n-m,3)$ is 1 or 2. In CP spectroscopy, we find that a strong signal is obtained when we pump at the allowed nanotube E_{ii} optical transitions. We found experimentally that, for the RBM modes, the CP intensity within a mod 2 family tends to decrease with chiral angle and the decrease in CP intensity with chiral angle is found to be much more pronounced for the E_{11} feature. We also found that CP intensities are considerably weaker in mod 1 families in comparison with mod 2 families. In general, the E_{22} CP intensities in mod 2 families are stronger than the E_{11} features while the opposite is true in mod 1 tubes. For RBM modes in mod 1 tubes, the E_{11} CP intensities tend to decrease with increasing chiral angle within a given family. As the family index $(2n+m)$ increases, the E_{11} CP intensity in mod 1 tubes decreases. Finally, we compared our theoretical results with experimental CP spectra in mod 2 nanotubes and found that our theoretical model correctly predicts the experimentally observed overall trends in the relative strengths of the CP signal both within and between mod 2 families. We found discrepancies between our theoretical predictions with regard to the peak positions and line shapes. These discrepancies can be qualitatively attributed to Coulomb interactions which have not yet been included in the calculations.

We do not consider the Coulomb interaction and excitonic effects in our theoretical model for reasons of simplicity and tractability. It has been pointed out that excitonic effects are important for understanding the optical properties of small-diameter carbon nanotubes.[16] In a number of Raman scattering theories the Coulomb interaction is neglected, but nevertheless the computed RBM Raman spectra can explain many experimental measurements.[17–19] It is worth dwelling a little on the reason for this. Jiang *et al.*[10] recently undertook a study of the exciton-photon and exciton-phonon matrix elements in single-walled carbon nanotubes using a tight-binding model. These authors found that for the RBM and *G*-band modes, the phonon matrix elements in the exciton and free-particle pictures are nearly the same. However, values for the exciton-photon matrix elements are on the order of 100 times greater than the electron-photon matrix elements computed in the free-particle picture. Thus, when we discuss the photoexcitation of carriers, the actual photoexcited carrier densities will be different from what we predict. On the other hand when we discuss the dependence of the coherent phonon amplitudes on the E_{ii} transition energies or the tube chirality, the present discussion has a physical meaning. Thus we expect reasonable agreement between experiment and theory for relative coherent phonon amplitudes and the relative strengths of the computed CP spectra. However, the peak positions and line shapes of the CP spectra will be altered by the neglect of excitonic effects.

Apart from being useful in resonant CP spectroscopy of chirality-specific nanotubes, we note that laser-induced coherent phonons in carbon nanotubes may also have important practical applications in the fabrication of carbon nanotube electronic devices. In recent years laser-induced coherent phonon generation has been theoretically studied using molecular-dynamics techniques.[20–24] Garcia *et al.*[21] simulated laser-induced coherent phonons in a mod 1 zigzag (10,0) capped carbon nanotube using a formalism that combines a nonadiabatic molecular-dynamics method and a density matrix approach to describe the dynamics of the carbon ions and valence electrons. Dumitrică *et al.*[22,23] theoretically studied the possibility of achieving selective cap opening in (10,0), (5,5), and (8,4) capped carbon nanotubes driven by laser-induced coherent phonons using nonadiabatic molecular-dynamics simulations based on a microscopic electronic model.

It is well known that self-assembled carbon nanotubes suffer from structural imperfections that modify their electronic, optical, and mechanical properties. Such defects pose a problem for the fabrication of nanotube-based electronic devices.[24] A common type of defect in carbon nanotubes is the (5-7) pair defect introduced by applying a Stone-Wales transformation to the nanotube structure.[20] In the Stone-Wales transformation, four hexagons are replaced with two pentagons and two heptagons.[25] The possibility of eliminating such defects using laser-generated coherent phonons has been studied theoretically in armchair and zigzag nanotubes using nonadiabatic molecular-dynamics simulations. Romero *et al.*[24] studied the response of armchair nanotubes with (5-7) pair defects to ultrafast laser pulses and found that when the fraction of photoexcited electrons exceeds a critical threshold (around 7%) the resulting coherent phonon oscillations cause the nanotube to undergo an inverse Stone-Wales structural transition that heals the defect. More recently Valencia *et al.*[20] extended these studies to zigzag nanotubes and found similar results.

Recently, Jeschke *et al.*[26] theoretically studied the structural response of nanotubes of different chiralities to femtosecond laser excitation using molecular-dynamics simulations. They found that carbon nanotubes may transform into more stable structures under the appropriate conditions. Such investigations may be important for technological applications. For example, nanotubes excited by lasers above a certain threshold may tear open and interact with other tubes leading to the creation of new structures.

II. EXPERIMENT

In this section, we demonstrate the implementation of ultrafast pulse shaping to excite the coherent radial breathing modes of specific chiralities, providing a definitive ability to study single-chirality nanotubes from an ensemble sample. Our method exploits selective excitation not only to extract chiral-dependent band-gap modulations but also utilizes information from the probe energy dependence of the phase and the amplitude of the coherent phonon oscillations to re-

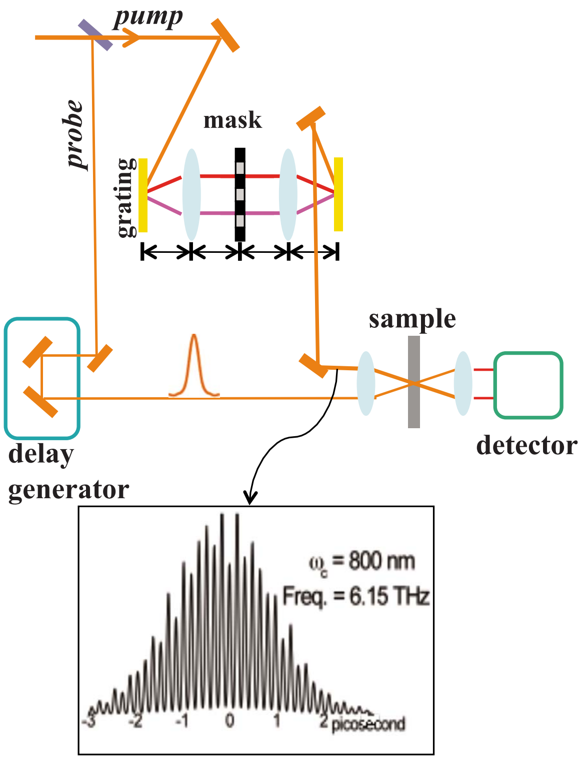

FIG. 1. (Color online) Experimental setup for chirality-selective excitation of coherent lattice vibrations in single-walled carbon nanotubes through ultrafast pulse shaping. The inset shows an example of multiple pulse trains with a repetition rate of 6.15 THz and a central wavelength of 800 nm (1.55 eV).

construct excitation profiles for the E_{22} transitions. In particular, our observation of probe-energy-dependent phase reversal provides direct time-domain evidence that for coherent radial breathing modes the band gap oscillates in response to the nanotube diameter oscillations.

The sample used in this study was a micelle-suspended SWNT solution, where the single-walled carbon nanotubes (HiPco batch HPR 104) were suspended as individuals with sodium cholate. The optical setup was that of standard degenerate pump-probe spectroscopy, but chirality selectivity of RBM oscillations was achieved by using multiple pulse trains, with a pulse-to-pulse interval corresponding to the period of a specific RBM mode.[15] Among different species of nanotubes, those having RBM frequencies that are matched to the repetition rate of multiple pulse trains will generate large amplitude coherent oscillations with increasing oscillatory response to each pulse, while others will have diminished coherent responses.[11–13] The tailoring of multiple pulse trains from femtosecond pulses was achieved using the pulse-shaping technique developed by Weiner and Leaird.[27] As depicted in Fig. 1, pulse trains are incident on an ensemble of nanotubes as a pump beam, whereas coherent RBM oscillations are monitored by an unshaped Gaussian probe beam.

Real-time observation of coherent RBM oscillations is possible without pulse shaping by employing standard femtosecond pump-probe spectroscopy.[11,13] Figure 2(a) shows transmission modulations of the probe beam induced by coherent lattice modulations, which were generated by pump pulses with a pulse width of 50 fs and a central wavelength of 800 nm (1.55 eV). The time-domain beating profiles reflect the simultaneous generation of several RBM frequencies from nanotubes in the ensemble with different chiralities, which are clearly seen in Fig. 2(b) with the Fourier transformation of the time-domain data. Although resonance conditions and mode frequencies lead to the assignment of chiralities to their corresponding peaks,[12] obtaining detailed information on dynamical quantities such as the phase information of phonon oscillations becomes rather challenging. Additionally, if adjacent phonon modes overlap in the spectral domain, this can lead to peak distortions.

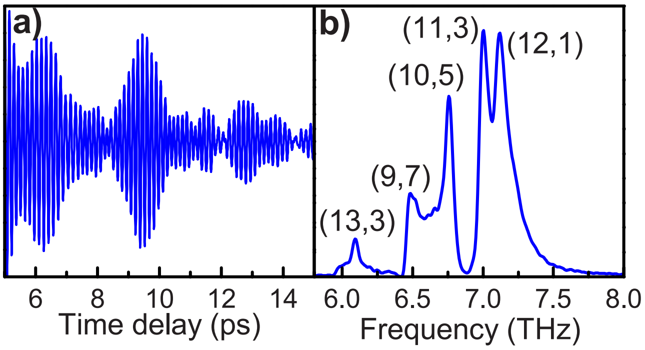

FIG. 2. (Color online) Generation and detection of coherent phonons of the radial breathing mode in single-walled carbon nanotubes. (a) Time-domain transmission modulations due to coherent RBM vibrations in ensemble single-walled carbon nanotube solution that were generated by standard pump-probe spectroscopy without pulse shaping. (b) Fourier transformation of time-domain oscillations with chirality assigned peaks.

However, by introducing pulse shaping, multiple pulses with different repetition rates are used to excite RBM oscillations and, as shown in Figs. 3(a)–3(d), chirality selectivity was successfully obtained. With the appropriate repetition rate of the pulse trains, a single specific chirality dominantly contributes to the signal, while other nanotubes are suppressed. For example, by choosing a pump repetition rate of 7.07 THz, we can selectively excite only the (11,3) nanotubes, as seen in Fig. 3(a). Similarly, with a pump repetition rate of 6.69 THz, the (10,5) nanotubes are selectively excited, as seen in Fig. 3(b). The accuracy of selectivity depends on the number of pulses in the tailored pulse train as well as the distribution of chiralities in the nanotubes ensemble. Furthermore, selective excitation of a specific chirality also requires the pump energy to be resonant with the corresponding E_{22} transition for each chirality-specific nanotubes.

The ability to excite single-chirality nanotubes allows us to perform detailed studies of excited states of single-walled carbon nanotubes. For example, by placing a series of 10 nm bandpass filters in the probe path before the detector, we can measure the wavelength dependence of RBM-induced transmission changes in order to understand exactly how the tube diameter changes during coherent phonon RBM oscillations and how the diameter change modifies the nanotube band structure. As seen in Fig. 4, the differential transmission is shown for three cases, from top to bottom, corresponding to

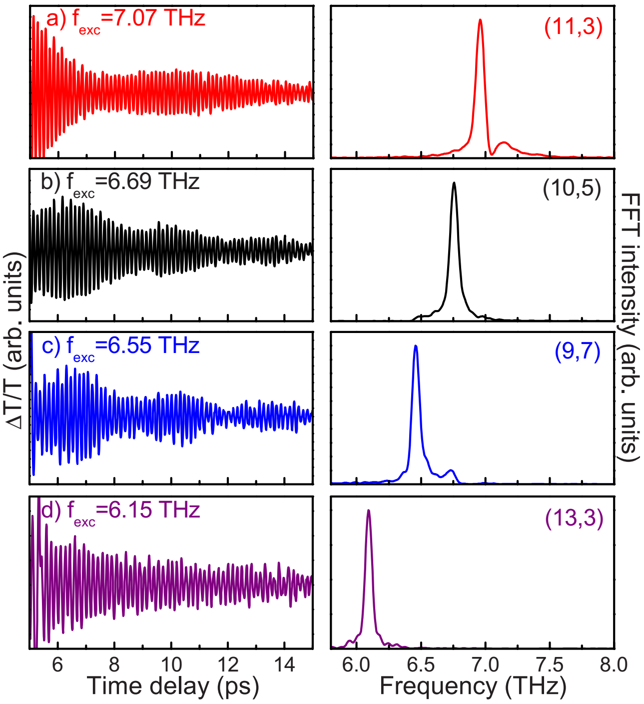

FIG. 3. (Color online) (Left) Time-domain coherent RBM oscillations selectively excited by multiple pulse trains via pulse shaping with corresponding repetition rates from 6.15 to 7.07 THz. (Right) Fourier transformations of corresponding oscillations, with their dominant nanotube chirality (n,m) indicated.

probe photon energies above, on, and below resonance, respectively, for selectively excited (11,3) carbon nanotubes. Although the transmission is strongly modulated at the RBM frequency (7.07 THz) for all three cases, the amplitude and phase of oscillations vary noticeably for varying probe wavelengths. Specifically, the amplitude of oscillations becomes minimal at resonance and, in addition, there is clearly a π-phase shift between the above- and below-resonance traces. Because the band-gap energy and diameter are inversely related to each other, and because it is the RBM frequency at which the diameter is oscillating, we can conclude from this data that the energy of the E_{22} resonance is oscillating at the RBM frequency. Namely, when the band gap is decreasing, absorption above (below) resonance is decreasing (increasing), resulting in positive (negative) differential transmission.

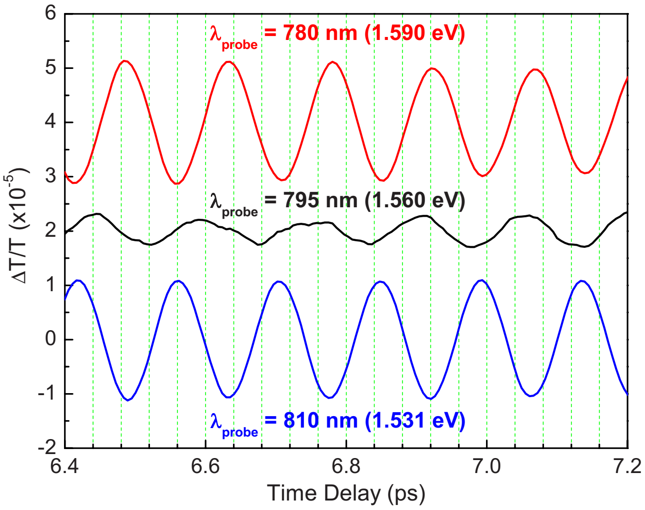

FIG. 4. (Color online) Differential transmission as a function of time delay at probe wavelengths of 780, 795, and 810 nm for the selective RBM excitation of the (11,3) nanotubes. There is a π phase shift between the 780 and 810 nm data. These three wavelengths (from the top to the bottom of the figure) correspond to photon energies above, at, and below the energy of the second exciton resonance, respectively, of (11,3) nanotubes.

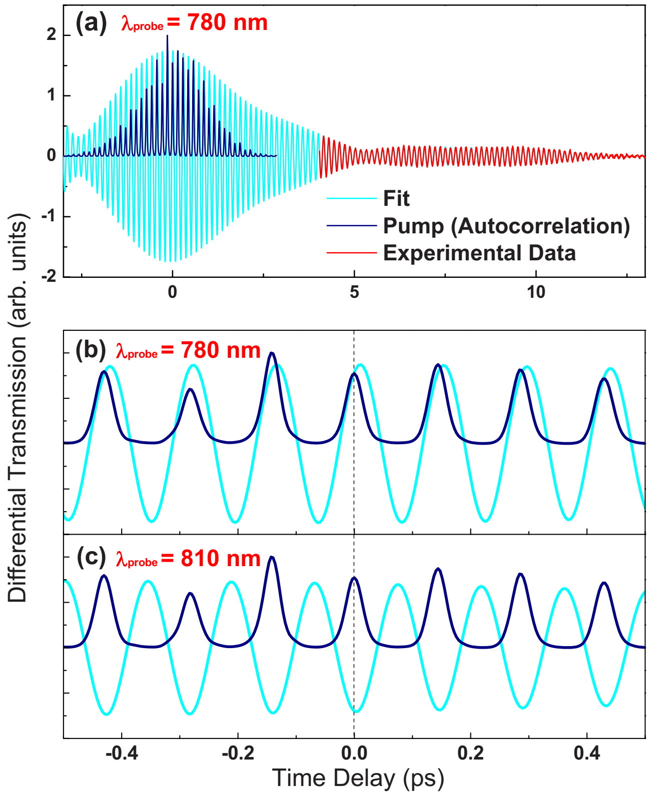

FIG. 5. (Color online) (a) Differential transmission as a function of time delay together with the pump pulse train (dark blue or dark gray) as well as fit (light blue or light gray up to 4 ps) to exponentially decaying sinusoidal oscillations. [(b),(c)] Data near time zero for two wavelengths corresponding to energies above and below the second exciton resonance, respectively, of (11,3) nanotubes.

We can also look at the short response to see how the diameter changes in response to ultrafast excitation of electron-hole pairs by the pump pulse. In Fig. 5(a), we plot the differential transmission data taken at 780 nm (1.59 eV) together with the pump pulse train, with time zero corresponding to the center of the pulse train. Here we note that an increase in the absorption corresponds to a decrease in the differential transmission. Figures 5(b) and 5(c) show data near time zero for two wavelengths corresponding to energies above and below the second exciton resonance, respectively, of (11,3) nanotubes. The sign of the differential transmission oscillations in the first quarter period, where the time delay varies from 0.0 to 0.07 ps, is positive (negative) for the above (below) resonance probe, indicating that there is an initial decrease (increase) in absorption for energies above (below) resonance, demonstrating that the diameter of the nanotube initially expands, taking into account the fact that the resonance energy is inversely related to the diameter. This initial expansion of the tube diameter is in agreement with our theoretical predictions for the photoexcitation of coherent phonon RBM oscillations by ultrafast laser pulses pumping near the E_{22} transition energy in mod 2 nanotubes [e.g., (11,3) tubes].

III. THEORY

We have developed a microscopic theory for the generation of coherent phonons in single-walled carbon nanotubes and their detection by means of coherent phonon spectroscopy experiments. Our approach is based on obtaining equations of motion for the coherent phonon amplitudes from the Heisenberg equations of motion as described by Kuznetsov and Stanton in Ref. 28. In our theoretical model, we explicitly incorporate the electronic energies and wave functions for the π electrons, the phonon-dispersion relations and the corresponding phonon modes, the electron-phonon interaction, the optical matrix elements, and the interaction of carriers with a classical ultrafast laser pulse. For simplicity, and to make the problem tractable, we neglect the many-body Coulomb interaction and interactions with the surrounding liquid medium in the micelle-suspended nanotube ensemble.

We are able to treat nanotubes of arbitrary chirality by exploiting all the screw symmetry operations. This allows us to examine trends in the CP signal strength within and between nanotube families. In addition, we gain something in our conceptional understanding by deriving a simple driven oscillator equation for the coherent phonon amplitudes where the driving function depends explicitly on the time-dependent photoexcited carrier distribution functions. In the limit where we ignore Coulomb interactions, the driven oscillator equation for the coherent phonon amplitudes turns out to be exact.[28]

A. Electron Hamiltonian

We treat carbon nanotube π and π^* electronic states in the ETB formalism of Porezag *et al.*[29] In the ETB model, the tight-binding Hamiltonian and overlap matrix elements between π orbitals on different carbon atoms are functions of the interatomic distance. The position-dependent Hamiltonian and overlap matrix elements are obtained from a parametrization of density-functional theory (DFT) results in the local-density approximation (LDA) using a local orbital basis set as described in Ref. 29. Our computed energy dispersion relations for the bonding π and antibonding π^* bands in graphene are plotted in Fig. 6 along high-symmetry directions in the hexagonal two-dimensional Brillouin zone. For comparison, we also plot the graphene energy dispersion relations obtained from the simple tight-binding model (STB), described in Ref. 1, in which only nearest-neighbor Hamiltonian and overlap matrix elements are considered. In the STB model, the values of the nearest-neighbor Hamiltonian and overlap matrix elements are −3.033 eV and 0.129, respectively.[1] The ETB and STB models agree with each other near the K and K' points in the Brillouin zone and in carbon nanotubes these are the states that give rise to the low-lying conduction and valence subbands that we are interested in.

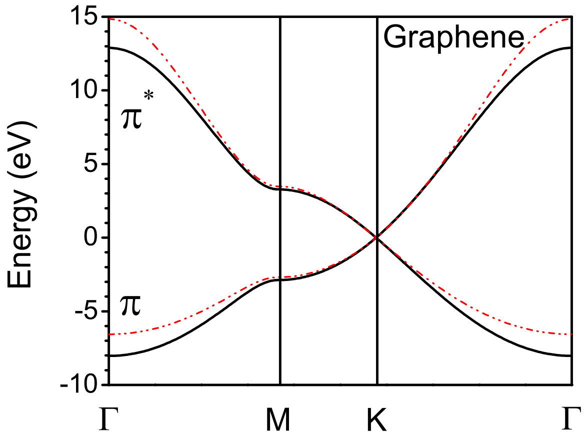

FIG. 6. (Color online) Extended tight-binding energy dispersion relations for the bonding π and antibonding π^* bands in graphene along high-symmetry directions in the Brillouin zone are shown as solid black lines. Energy dispersion relations in the nearest-neighbor tight-binding model described in Ref. 1 are shown as dashed-dotted red lines.

In a carbon nanotube with chiral indices (n,m), a translational unit cell can be found such that the atomic structure repeats itself after translation of the tube by a translational vector $\mathbf{T}$ parallel to the tube axis.[1] The resulting Brillouin zone is one dimensional with $|k| \leq \pi/T$ and the number of two-atom hexagonal cells in each translational unit cell is[1]

$$N_{\text{hex}} = \frac{2(n^2 + nm + m^2)}{\gcd(2n + m, 2m + n)}, \tag{1}$$

where $\gcd(i,j)$ is the greatest common divisor of integers i and j. If we only make use of translational symmetry in formulating the electronic problem, the resulting size of the Hamiltonian and overlap matrices is $2N_{\text{hex}} \times 2N_{\text{hex}}$ if we retain one π orbital per site.

In practice, the size of the electronic Hamiltonian and overlap matrices obtained using the nanotube translational unit cell can become prohibitively large, especially for chiral nanotubes with $n > m \neq 0$. Fortunately, we can reduce the size of the electronic problem by further exploiting the symmetry of the nanotube. As pointed out in Ref. 17 a two-atom hexagonal unit cell in graphene, with the two carbon atoms labeled A and B, can be mapped onto the nanotube by applying two different screw operations. If we make use of the screw symmetry operations, we can block diagonalize the $2N_{\text{hex}} \times 2N_{\text{hex}}$ Hamiltonian and overlap matrices into 2×2 sub-blocks which we label μ. In carbon nanotubes, the subblock index μ labels the cutting lines in the zone folding picture. For states near the Fermi energy, the cutting line numbers μ have a nice geometrical interpretation as pointed out in Ref. 30.

Derivations for the Hamiltonian and overlap matrices for the electronic states in a carbon nanotube are given in Appendix A. We let $s = v, c$ label the valence and conduction-

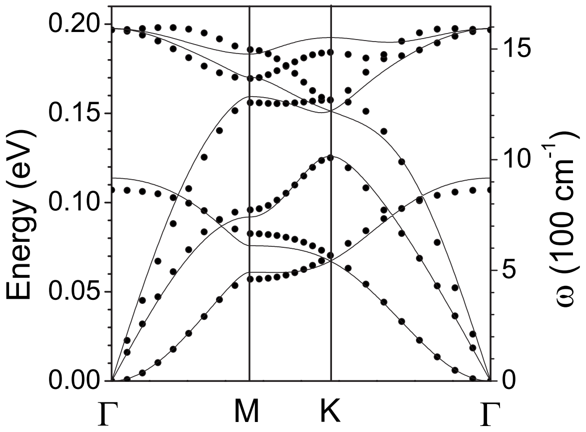

FIG. 7. Graphene phonon-dispersion relation. The solid circles are the valence force field model of Jishi *et al.* (Ref. 35) and the solid lines are the best fit results for our seven-parameter valence force field model.

band states and the electronic energies $E_{s\mu}(k)$ for a given cutting line are obtained by solving the matrix eigenvalue problem in Eq. (A8). The second-quantized electron Hamiltonian is simply

$$\hat{H}_e = \sum_{s\mu k} E_{s\mu}(k) c^{\dagger}_{s\mu k} c_{s\mu k}, \tag{2}$$

where $c^{\dagger}_{s\mu k}$ creates an electron in the state with energy $E_{s\mu}(k)$.

B. Phonon Hamiltonian

Following Jiang *et al.*[31] and Lobo and Martins,[32] we treat lattice dynamics in a carbon nanotube using a valence force field model. In our force field model, we include bond stretching, in-plane bond bending, out-of-plane bond bending, and bond twisting potentials. In constructing the valence force field potentials, we take care that they satisfy the force constant sum rule which requires that the force field potential energy remain invariant under rigid translations and rotations (see Ref. 33, p. 131). As pointed out in Ref. 34, a number of calculations in the literature use force field models that violate the force constant sum rule and, as a result, fail to reproduce the long wavelength flexure modes predicted by elasticity theory.

Our valence force field model as described in Appendix B has seven force constants, four due to bond stretching interactions out to fourth nearest-neighbor shells and one each from the remaining three interactions. To determine these seven force constants, we fit our model results for planar graphene to the model of Jishi *et al.*[35] Our best fit dispersion relations are shown in Fig. 7 as solid lines while the results of Jishi *et al.* are shown as solid circles.

We should point out that since our force field model contains force constants that are independent of the density of photoexcited carriers, it cannot describe phonon softening which is observed at high values of the laser fluence. However, a rather high value of the laser fluence is generally needed to generate a high density of photoexcited carriers. In the case of metallic nanotubes, the chirality-dependent frequency shift of the RBM and G modes has been studied by Sasaki *et al.* in Refs. 36 and 37 as a function of the Fermi energy. In the case of the RBM mode they find that armchair nanotubes do not exhibit any frequency shift while zigzag nanotubes exhibit phonon softening.[36]

The phonon energies and corresponding mode displacement vectors are obtained by diagonalizing the dynamical matrix. In graphene, there are two atoms per unit cell giving rise to the six phonon modes shown in Fig. 7. In a carbon nanotube, the size of the dynamical matrix is $6N_{\text{hex}} \times 6N_{\text{hex}}$. By making use of the nanotube screw symmetry operations, we can block diagonalize the dynamical matrix into 6×6 sub-blocks which we label $\nu = 0, \ldots, N_{\text{hex}}-1$. Again, the sub-block index ν labels the cutting lines. In a carbon nanotube, the phonon energies $\hbar\omega_{\beta\nu}(q)$ are obtained from solving the dynamical matrix eigenvalue problem in Eq. (B10) where ν is the cutting line index and $\beta = 1, \ldots, 6$ labels the six modes associated with each cutting line. The phonon wave vector q is defined on a one-dimensional Brillouin zone given by $|q| \leq \pi/T$.

The second-quantized phonon Hamiltonian is given by

$$\hat{H}_{\text{ph}} = \sum_{\beta\nu q} \hbar\omega_{\beta\nu}(q) b^{\dagger}_{\beta\nu q} b_{\beta\nu q}, \tag{3}$$

where $b^{\dagger}_{\beta\nu q}$ creates a phonon in a state with energy $\hbar\omega_{\beta\nu}(q)$.

C. Electron-phonon coupling

The position-dependent single-electron Hamiltonian for a single-walled carbon nanotube is given by

$$H(\mathbf{r}) = T_0 + \sum_{r\mathbf{J}} v_c[\mathbf{r} - (\mathbf{R}_{r\mathbf{J}} + \mathbf{U}_{r\mathbf{J}})], \tag{4}$$

where the kinetic energy is T_0 and $v_c(\mathbf{r})$ is the carbon atom potential. In Eq. (4) $\mathbf{R}_{r\mathbf{J}}$ is the equilibrium position of the rth atom in the $\mathbf{J}$th two-atom unit cell and $\mathbf{U}_{r\mathbf{J}}$ is the corresponding atomic displacement from equilibrium as defined in Appendix B.

Expanding this Hamiltonian in a Taylor series to first order in the atomic displacements, we obtain a position-dependent electron-phonon interaction Hamiltonian,

$$H_{ep}(\mathbf{r}) = -\sum_{r\mathbf{J}} \nabla v_c(\mathbf{r} - \mathbf{R}_{r\mathbf{J}}) \cdot \mathbf{U}_{r\mathbf{J}}. \tag{5}$$

Starting from the classical symmetry-adapted atomic displacement in Eq. (B7) of Appendix B, we make the transition to quantum mechanics and define a symmetry-adapted second-quantized phonon displacement operator,

$$\hat{\mathbf{U}}_{r\mathbf{J}} = \sum_{\beta\nu q} A_{\beta,\nu}(q) S(\theta_{\mathbf{J}}) \hat{\mathbf{e}}_r(\beta,q,\nu) e^{i\phi_{\mathbf{J}}(q,\nu)} (b_{\beta\nu q} + b^{\dagger}_{\beta\nu,-q}) \tag{6}$$

with the quantized phonon amplitudes

$$A_{\beta,\nu}(q) = \frac{1}{2} \frac{\hbar}{\sqrt{M N_{\text{hex}} \hbar\omega_{\beta\nu}(q)}}. \tag{7}$$

Using the phonon displacement operator in Eq. (6) we arrive at the desired second-quantized electron-phonon Hamiltonian,

$$\hat{H}_{ep} = \sum_{ss'\beta}\sum_{\mu\nu}\sum_{kq} M^{\mu,\nu}_{s,s',\beta}(k,q)\, c^{\dagger}_{s',\mu+\nu,k+q}\, c_{s\mu k}(b_{\beta\nu q} + b^{\dagger}_{\beta\nu,-q}). \tag{8}$$

The first term in the electron-phonon Hamiltonian [Eq. (8)] is proportional to the operator $c^{\dagger}_{s',\mu+\nu,k+q}c_{s\mu k}b_{\beta\nu q}$. This term describes a phonon absorption process in which an electron with energy $E_{s\mu}(k)$ absorbs a phonon with energy $\hbar\omega_{\beta\nu}(q)$ and then scatters into the state with energy $E_{s',\mu+\nu}(k+q)$. Likewise, the second term in Eq. (8) describes a phonon emission process.

Details concerning the evaluation of the electron-phonon interaction matrix elements $M^{\mu,\nu}_{s,s',\beta}(k,q)$ are given in Appendix C. In evaluating these matrix elements, we make explicit use of $2p_z$ atomic wave functions and screened atomic potentials obtained from an *ab initio* calculation in graphene.

D. Coherent phonon generation

The second-quantized phonon displacement operators in Eq. (6) are defined in terms of a sum over phonon modes of the second-quantized operator $b_{\beta\nu q}+b^{\dagger}_{\beta\nu,-q}$. For each phonon mode in the nanotube we are thus motivated to define a coherent phonon amplitude given by[28]

$$Q_{\beta\nu q}(t) = \langle b_{\beta\nu q}(t) + b^{\dagger}_{\beta\nu,-q}(t)\rangle,$$

where $\langle\ \rangle$ denotes the statistical average. Equations of motion for $Q_{\beta\nu q}(t)$ can be obtained from the phonon and electron-phonon Hamiltonians in Eqs. (3) and (8). From the Heisenberg equation we obtain

$$\frac{\partial^2 Q_{\beta\nu q}(t)}{\partial t^2} + \omega^2_{\beta\nu}(q)Q_{\beta\nu q}(t) = -\frac{2\omega_{\beta\nu}(q)}{\hbar}\sum_{ss'\mu k} M^{\mu,\nu}_{s,s',\beta}(k,-q)\langle c^{\dagger}_{s',\mu+\nu,k-q}(t)c_{s\mu k}(t)\rangle. \tag{9}$$

In coherent phonon spectroscopy, we assume that the optical pulse and hence the distribution of photoexcited carriers is spatially uniform over the nanotube. In this case the electronic density matrix is diagonal and can be expressed as

$$\langle c^{\dagger}_{s',\mu+\nu,k-q}(t)c_{s\mu k}(t)\rangle = \delta_{s,s'}\delta_{\nu,0}\delta_{q,0}f_{s\mu}(k,t), \tag{10}$$

where $f_{s\mu}(k,t)$ is the electron distribution function in subband $s\mu$ with wave vector k.[28]

The only coherent phonon modes that are excited are the $\nu=q=0$ modes whose amplitudes satisfy a driven oscillator equation,

$$\frac{\partial^2 Q_{\beta}(t)}{\partial t^2} + \omega^2_{\beta}Q_{\beta}(t) = S_{\beta}(t), \tag{11}$$

where $Q_{\beta}(t)\equiv Q_{\beta 00}(t)$ and $\omega_{\beta}\equiv\omega_{\beta,0}(q=0)$. There is no damping term in Eq. (11) since the anharmonic terms in the electron-phonon Hamiltonian are neglected. We solve the driven oscillator equation subject to the initial conditions $Q_{\beta}(0)=\dot{Q}_{\beta}(0)=0$. Taking the initial condition into account, the driving function $S_{\beta}(t)$ is given by

$$S_{\beta}(t) = -\frac{2\omega_{\beta}}{\hbar}\sum_{s\mu k} M^{\beta}_{s\mu}(k)[f_{s\mu}(k,t) - f^{0}_{s\mu}(k)], \tag{12}$$

where $f_{s\mu}(k,t)$ are the time-dependent electron distribution functions, $f^{0}_{s\mu}(k)$ are the initial equilibrium electron distribution functions, and $M^{\beta}_{s\mu}(k)\equiv M^{\mu 0}_{ss\beta}(k,q=0)$.

The coherent phonon driving function $S_{\beta}(t)$ depends on the photoexcited electron distribution functions. In principle, we could solve for the time-dependent distribution functions in the Boltzmann equation formalism taking photogeneration and relaxation effects into account. In CP spectroscopy, an ultrafast laser pulse generates electron-hole pairs on a time scale, short in comparison with the coherent phonon period. In our experimental work, we typically use 50 fs ultrafast laser pulses to excite RBM coherent phonons with oscillation periods of around 0.14 ps ($\hbar\omega_{\beta}\approx 30$ meV or 242 cm^{-1}).

After photoexcitation the electron-hole pairs slowly scatter and recombine. Jiang *et al.*[38] recently carried out a study of the electron-phonon interaction and relaxation time in graphite and found relaxation times on the order of a few picoseconds which is much slower than either the ultrafast laser pulse or the RBM coherent phonon oscillation period. The driving function $S_{\beta}(t)$ thus rises sharply in a steplike fashion and then slowly vanishes as the distribution functions $f_{s\mu}(k,t)$ return to $f^{0}_{s\mu}(k)$. The rapid initial jump in $S_{\beta}(t)$ gives rise to an oscillatory part of the coherent phonon amplitude $Q_{\beta}(t)$ at the coherent phonon frequency ω_{β}, while the slow subsequent decay of $S_{\beta}(t)$ gives rise to a slowly varying background. Since the observed CP signal is proportional to the power spectrum of the oscillatory part of $Q_{\beta}(t)$, we choose to ignore relaxation effects and retain only the rapidly varying photogeneration term in the Boltzmann equation. Neglecting carrier relaxation will have a negligible effect on the computed CP signal since the relaxation time is much greater than the coherent phonon period.

The photogeneration rate in the Boltzmann equation depends on the polarization of the incident ultrafast laser pulse. Using an effective-mass model, Ajiki and Ando[39] showed that optical absorption in an isolated single-walled carbon nanotube for polarization perpendicular to the nanotube axis is almost perfectly suppressed by photoinduced charge (the depolarization effect). Recently, Popov and Henrard[40] undertook a comparative study of the optical properties of carbon nanotubes in orthogonal and nonorthogonal tight-binding models and found that optical absorption due to light polarized parallel to the tube axis (z axis) is greater than absorption due to light polarized perpendicular to the axis by about a factor of 5. Consequently we confine our attention to light polarized parallel to the tube axis only. We compute the photogeneration rate in the electric dipole approximation using Fermi's golden rule. In the case of parallel polarization, optical transitions can only occur between states with the same angular-momentum quantum number μ.[17,40] For the photogeneration rate we find

$$\left.\frac{\partial f_{s\mu}(k)}{\partial t}\right|_{\text{gen}} = \frac{8\pi^2 e^2 u(t)}{\hbar n_g^2(\hbar\omega)^2}\left(\frac{\hbar^2}{m_0}\right)\sum_{s'}|P^{\mu}_{ss'}(k)|^2[f_{s'\mu}(k,t) - f_{s\mu}(k,t)]\,\delta(\Delta E^{\mu}_{ss'}(k)-\hbar\omega), \tag{13}$$

where $\Delta E^{\mu}_{ss'}(k)=|E_{s\mu}(k)-E_{s'\mu}(k)|$ are the k-dependent transition energies, $\hbar\omega$ is the pump energy, $u(t)$ is the time-dependent energy density of the pump pulse, e is the electron charge, m_0 is the free electron mass, and n_g is the index of refraction in the surrounding medium. The optical matrix element is given by

$$P^{\mu}_{ss'}(k) = \frac{\hbar}{\sqrt{2}m_0}\sum_{r'} C^*_{r'}(s',\mu,k)\sum_{r\mathbf{J}} C_r(s,\mu,k)e^{i\phi_{\mathbf{J}}(k,\mu)}M_z(r',r\mathbf{J}), \tag{14}$$

where the sum over $r\mathbf{J}$ is taken over fourth nearest neighbors of the atom at $\mathbf{R}_{r'0}$. In Eq. (14), $C_r(s,\mu,k)$ are the expansion coefficients for the symmetry-adapted ETB wave functions obtained by solving the matrix eigenvalue problem in Eq. (A8) of Appendix A and $\phi_{\mathbf{J}}(k,\mu)$ is the phase factor defined in Eq. (A7).

The z components of the atomic dipole matrix elements (which can be evaluated analytically) are given by

$$M_z = \int d\mathbf{r}\; \varphi^*_{r'0}(\mathbf{r}-\mathbf{R}_{r'0})\frac{\partial}{\partial z}\varphi_{r\mathbf{J}}(\mathbf{r}-\mathbf{R}_{r\mathbf{J}}), \tag{15}$$

where the $2p_z$ orbitals $\varphi_{r\mathbf{J}}$ are defined in Eq. (C3). Note that the squared optical matrix element $|P^{\mu}_{s,s'}(k)|^2$ has units of energy. We point out that optical dipole matrix elements in the vicinity of the K point in both graphite and carbon nanotubes have been studied previously in Ref. 41.

The pump energy density $u(t)$ is related to the fluence $F = \int dt\; u(t)(c/n_g)$. To simplify our theoretical model, it is assumed that the pump beam consists of a train of N_{pulse} identical Gaussian pulses each with an intensity full width at half maximum (FWHM) of τ_p and a Lorentzian spectral line shape with a FWHM of Γ_p. The Gaussian pulses are equally spaced in time with the time interval between pulses being T_{pulse}. The peak intensity of the first pulse is taken to occur at $t=0$. To account for spectral broadening of the laser pulses we replace the delta function in Eq. (13) with[42]

$$\delta(\Delta E - \hbar\omega) \to \frac{\Gamma_p/(2\pi)}{(\Delta E - \hbar\omega)^2 + (\Gamma_p/2)^2}. \tag{16}$$

From the coherent phonon amplitudes, the time-dependent macroscopic displacements of each carbon atom in the nanotube can be obtained by averaging Eq. (6). Thus

$$\mathbf{U}_{r\mathbf{J}}(t) = \sum_{\beta} A_{\beta}S(\theta_{\mathbf{J}})\hat{\mathbf{e}}^{\beta}_{r}Q_{\beta}(t), \tag{17}$$

where $A_\beta \equiv A_{\beta,0}(0)$ and $\hat{\mathbf{e}}^{\beta}_{r} \equiv \hat{\mathbf{e}}_r(\beta,0,0)$.

It is apparent that only four coherent phonon modes can be excited in a carbon nanotube regardless of the chirality. Since $\nu=q=0$ the CP active mode frequencies and polarization vectors are found by diagonalizing a single 6×6 dynamical matrix in Eq. (B10). Two of the six mode frequencies ω_β are zero and these phonons are not excited since the driving term $S_\beta(t)$ vanishes as can be seen in Eq. (12). Of the remaining four modes, the one with the lowest energy is the radial breathing mode.

Coherent acoustic-phonon modes whose energies vanish at $q=0$ cannot be excited in an infinitely long carbon nanotube under conditions of uniform illumination by the pulse laser. If, however, the electric field of the pump laser could be made to vary spatially along the nanotube axis with a periodicity given by a real-space wave vector q_{pulse}, it would be possible to generate coherent acoustic phonons which would travel along the nanotube at the acoustic sound speed. The generation of coherent acoustic phonons has been demonstrated in semiconductor superlattices where the pump laser generates carriers in the quantum wells, thus giving rise to carrier distribution functions having the periodicity of the superlattice.[43–46] In the case of coherent acoustic phonons in superlattices, the coherent phonon lattice displacement satisfies a driven loaded string equation rather than a driven harmonic-oscillator equation.[43]

E. Absorption spectrum

In coherent phonon spectroscopy a probe pulse is used to measure the time-varying absorption coefficient of the carbon nanotube. The time-dependent absorption coefficient is given by[42,47]

$$\alpha(\hbar\omega,t) = \frac{\hbar\omega}{n_g\hbar c}\varepsilon_2(\hbar\omega,t), \tag{18}$$

where $\varepsilon_2(\hbar\omega,t)$ is the imaginary part of the time-dependent dielectric function evaluated at the probe photon energy $\hbar\omega$.

The imaginary part of the nanotube dielectric function is obtained from Fermi's golden rule,

$$\varepsilon_2(\hbar\omega) = \frac{8\pi^2e^2}{A_t(\hbar\omega)^2}\left(\frac{\hbar^2}{m_0}\right)\sum_{ss'\mu}\int\frac{dk}{\pi}|P^{\mu}_{ss'}(k)|^2[f_{s\mu}(k) - f_{s'\mu}(k)]\delta(E_{s'\mu}(k) - E_{s\mu}(k) - \hbar\omega), \tag{19}$$

where $A_t = \pi(d_t/2)^2$ is the cross-sectional area of the tube and d_t is the nanotube diameter. In our model, we replace the delta function in Eq. (19) with a broadened Lorentzian spectral line shape with a FWHM of Γ_s. The distribution function $f_{s\mu}(k)$ and band structure $E_{s\mu}(k)$ are time dependent. The time dependence of $f_{s\mu}(k)$ comes from the Boltzmann carrier dynamics which can include the photogeneration of electron-hole pairs as well as various carrier relaxation effects. The time dependence of $E_{s\mu}(k)$ arises from variations in the carbon-carbon bond lengths due to the coherent-phonon-induced atomic displacements $\mathbf{U}_{r\mathbf{J}}(t)$ given in Eq. (17). This time-dependent deformation of the nanotube bond lengths alters the tight-binding Hamiltonian and overlap matrix elements in the extended tight-binding model described in Sec. III A. Note that to first order in the lattice displacements the energies $E_{s\mu}(k)$ vary with time while the tight-binding wave functions and optical matrix elements $P^{\mu}_{ss'}(k)$ do not.

F. Coherent phonon spectrum

In the coherent phonon spectroscopy experiments described by Lim *et al.* in Refs. 12 and 13, single-color pump-probe experiments are performed on an ensemble of nanotubes. The excitation of coherent phonons by the pump modulates the optical properties of the nanotubes and gives rise to a transient differential transmission signal. After subtraction of a slowly varying background component, the coherent phonon spectrum is obtained by taking the power spectrum of the time-dependent differential transmission. In our model we simulate single-color pump-probe experiments and take the theoretical CP signal to be proportional to the power spectrum of the transient differential transmission after background subtraction. We compute the power spectrum using the Lomb periodogram algorithm described in Ref. 48. We find that using the Lomb periodogram to evaluate the power spectrum in our theoretical results is more convenient than using fast Fourier transform methods since it works well for data sets whose size is not an integer power of 2 or whose data points are not evenly spaced.

It is worth emphasizing that in CP spectroscopy we measure the power spectrum of the time-dependent coherent phonon-modulated differential transmission. Thus, as a function of the pump energy, the CP spectrum at the coherent phonon frequency tracks the absolute value of the first derivative of the static absorption coefficient. This is nicely illustrated in Fig. 6 of Ref. 12 where it is shown that an excitonic peak in the absorption spectrum will give rise to a symmetric double peaked structure in the CP power spectrum.

IV. THEORETICAL RESULTS

To illustrate our theoretical model, we will discuss in some details the simulated CP spectroscopy experiments in an undoped (11,0) zigzag nanotube. This is a mod 2 semiconducting nanotube with $\mathrm{mod}(n-m,3)=2$ belonging to the family of nanotubes with $2n+m=22$. We choose this example since we have performed CP spectroscopy for the (11,0) nanotube (see Fig. 18) and because Lim *et al.* measured coherent lattice vibrations in a micelle-suspended solution of carbon nanotubes with a diameter range of 0.7–1.3 nm (Refs. 12 and 13) and found strong CP signals due to excitation of coherent RBM modes in this family of nanotubes.

A. Band structure and absorption spectra

The four lowest-lying one-dimensional electronic π bands for the (11,0) nanotube are shown in the upper panel of Fig. 8. In our model we ignore structural optimization and assume that the carbon atoms lie on the surface of the rolled-up unreconstructed graphene cylinder. In an unreconstructed zigzag nanotube the length of the translational unit cell is $T=\sqrt{3}a$, where $a=2.49$ Å is the hexagonal lattice constant in graphene.[1] In Fig. 8 the conduction bands have positive energy and the valence bands have negative energy. Since the electronic problem has been reduced to solving the 2×2 matrix eigenvalue problem in Eq. (A8), the conduction bands in Fig. 8 with a given value of the angular quantum number μ can only mix with the valence band having the same value of μ. The four bands shown in the figure are doubly degenerate with two distinct values of μ giving rise to the same band energies. The allowed optical transitions for z-polarized light (with selection rule $\Delta\mu=0$) are indicated by vertical arrows and are labeled $E_{11},\ldots,E_{44}$.

The lower panel of Fig. 8 shows the square of the optical matrix elements defined in Eq. (14) for each of the transitions $E_{11},\ldots,E_{44}$. For the E_{11}, E_{22}, and E_{33} transitions the squared optical matrix elements are strongly peaked at the Van Hove singularity at the direct band gaps. The size of this peak in the squared optical matrix elements increases as the band gap moves away from the Fermi energy at $E=0$. The absorption for these three transitions are sharply peaked at the band edge due to the Van Hove singularity in the joint density of states as well as the peak in the squared optical matrix elements that occurs there. For the E_{44} transition, the conduction and valence bands are very flat giving rise to an enhanced Van Hove singularity in the joint density of states while the squared optical matrix element is a slowly varying function of k. For this transition, the peak in the absorption spectrum is due almost entirely to the sharply peaked joint density of states.

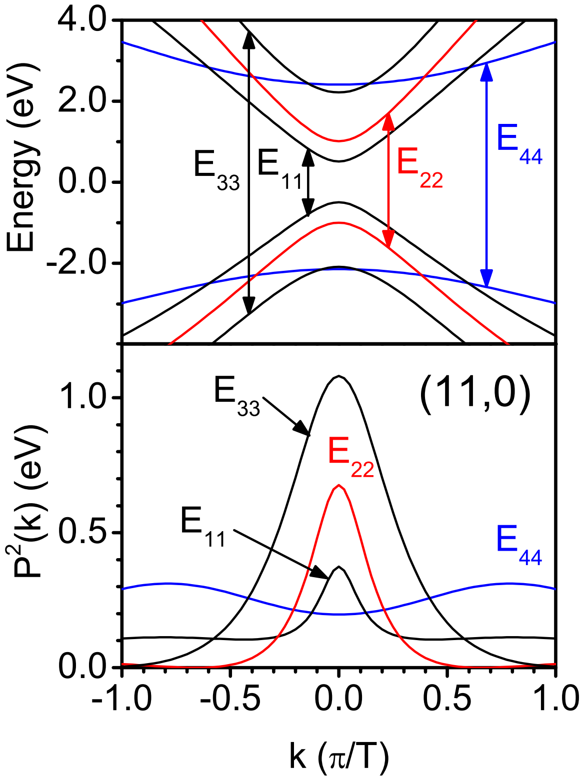

FIG. 8. (Color online) The upper panel show the four lowest-lying electronic π bands in the one-dimensional Brillouin zone for an (11,0) zigzag nanotube in the ETB model. All the bands are doubly degenerate. The allowed optical transition E_{ii} for light polarized along the tube axis is indicated. The lower panel shows the square of the optical matrix elements defined in Eq. (14) for each of the allowed optical transition.

As a check on our theoretically calculated squared optical matrix elements, we compared our results with optical dipole matrix elements calculated independently by Jiang *et al.* in Ref. 49 for the metallic (5,5) armchair and (6,0) zigzag tubes for light polarized parallel to the tube axis. Our squared optical matrix elements are proportional to the square of the dipole matrix elements shown in Figs. 2 and 3 in Ref. 49. We found excellent agreement between our theoretical results and the corresponding results for the two tubes considered.

With the electronic band structure and squared optical matrix elements shown in Fig. 8, we can obtain the absorption

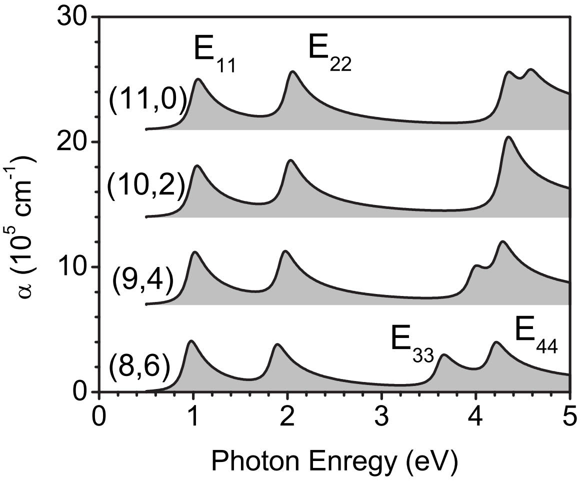

FIG. 9. Computed absorption coefficient as a function of photon energy for all nanotubes (n,m) in the family for which $2n+m=22$. The photons are assumed to be linearly polarized with the electric polarization vector parallel to the tube axis. Exciton effects are neglected.

coefficient of the (11,0) nanotube using Eqs. (18) and (19) and the carrier distribution functions. The computed absorption coefficient for the undoped (11,0) nanotube in thermal equilibrium at room temperature is shown in the upper curve of Fig. 9 where the spectral FWHM linewidth is taken to be $\Gamma_s=0.15$ eV. Also shown in the figure are the absorption spectra of the other members of family 22, namely, the (10,2), (9,4), and (8,6) nanotubes.

B. Generation of coherent RBM phonons

In a typical simulation, we excite coherent RBM phonons with a single 50 fs Gaussian laser pulse pumping at the peak of the broadened E_{22} transitions shown in Fig. 9. The pump fluence is taken to be 10^{-5} J/cm^2, the FWHM spectral linewidth is assumed to be $\Gamma_p=0.15$ eV, and the time scale is chosen so that the pump reaches its peak intensity at $t=0$. The pump energies $\hbar\omega$ at the E_{22} peaks are taken to be 2.05 eV for the (11,0) nanotube, 2.04 eV for (10,2), 1.97 eV for (9,4), and 1.89 eV for (8,6). The photogenerated carrier distribution functions are obtained from Eq. (13) and the photoexcited carrier densities per unit length are shown in Fig. 10 for family 22 nanotubes. The carrier densities after photoexcitation all lie in the range from 70 to 90 cm^{-1} increasing as we go from (11,0) to (8,6).

Using the photogenerated carrier densities $f_{s\mu}(k,t)$ we can obtain the coherent phonon amplitudes $Q_\beta(t)$ by solving the equation of motion (11) with the driving function $S_\beta(t)$ given in Eq. (12). As we noted earlier, β labels the six coherent phonon modes for each value of μ. Coherent phonon oscillations can only be excited in the four $q=0$ modes with nonzero frequency corresponding to $\mu=0$. The six $\mu=0$ phonon-dispersion curves are shown in Fig. 11 for the (11,0) nanotube. At $q=0$, there are two acoustic modes with zero frequency. The one with the lower sound speed is the twisting mode (TW) in which the A and B atom sublattices move in phase in the circumferential direction. The mode with the higher sound speed is the longitudinal acoustic (LA) mode in which the A and B atom sublattices move in phase along the tube axis. The remaining four $q=0$ modes are the CP active modes. The lowest CP active mode is the radial breathing mode at 37.1 meV (300 cm^{-1}) in which all the atoms move in phase radially in and out. The next highest CP active mode is the out-of-plane transverse optical (oTO) mode at 117 meV (944 cm^{-1}) in which the A atom sublattice moves radially outward as the B atom sublattice moves radially inward. There are two closely spaced high-frequency modes. The lower of these at 194.8 meV (1571 cm^{-1}) is the in-plane transverse optical (iTO) mode in which the A and B atom sublattices move in the circumferential direction out of phase with each other. The highest mode is the longitudinal optical (LO) mode at 197.9 meV (1596 cm^{-1}) in which the A and B atom sublattices move out of phase with each other along the tube axis.

In our model we neglect slow carrier relaxation effects and retain only the photogeneration term in the Boltzmann

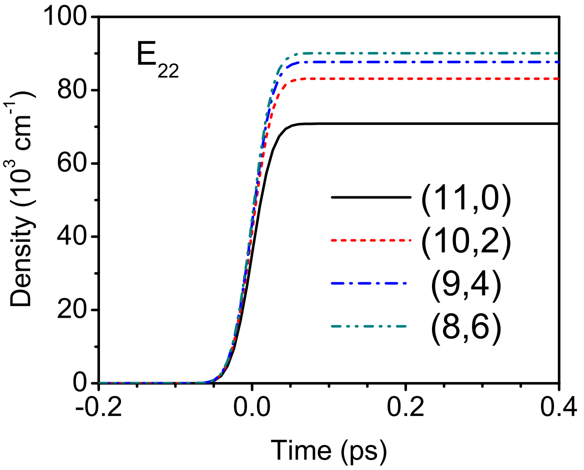

FIG. 10. (Color online) Computed photoexcited carrier density per unit length for nanotubes in family 22 after photoexcitation by a 50 fs Gaussian laser pulse with a fluence of 10^{-5} J/cm^2 pumping at the peak of the E_{22} features in Fig. 9.

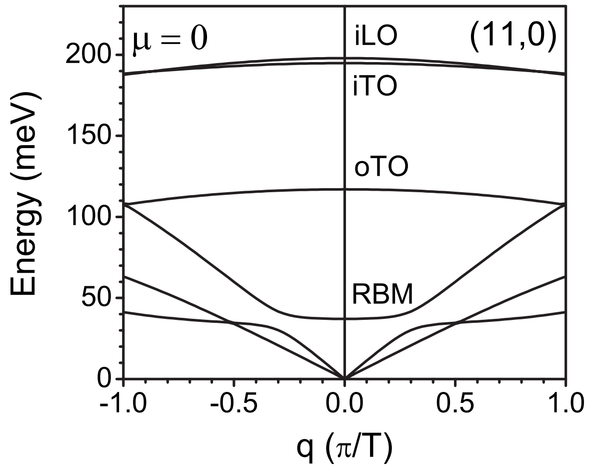

FIG. 11. Phonon-dispersion relations for $\mu=0$ phonons in (11,0) nanotubes. Only the four $q=0$ modes with nonzero frequency can be excited in coherent phonon spectroscopy.

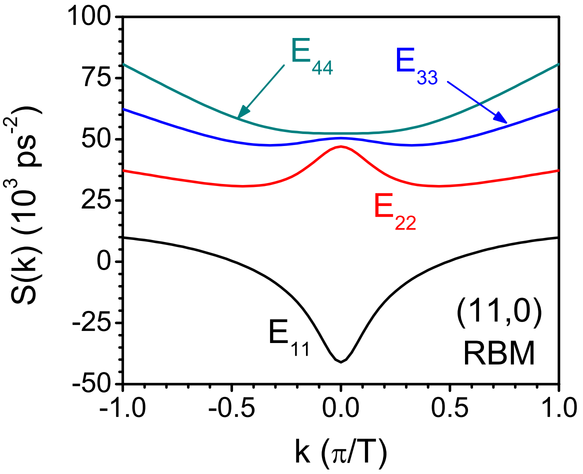

FIG. 12. (Color online) Driving function kernel for RBM coherent phonons in the (11,0) nanotube for several optical transitions E_{ii} in the impulsive excitation approximation.

equation. The net photogenerated conduction-band electron distribution function $f_{c\mu}(k)-f^0_{c\mu}(k)$ is then equal to the net photogenerated hole distribution function for each value of k. In this case, we can obtain a simplified expression for the coherent phonon driving function which only involves the photogenerated conduction-band electron distributions. We find

$$S_\beta(t) = \sum_{\mu k} S^\beta_\mu(k)[f_{c\mu}(k) - f^0_{c\mu}(k)]. \tag{20}$$

The driving function kernel $S^\beta_\mu(k)$ is given by

$$S^\beta_\mu(k) = -\frac{2\omega_\beta}{\hbar}[M^\beta_{c\mu}(k) - M^\beta_{v\mu}(k)], \tag{21}$$

where $M^\beta_{s\mu}(k)$ $(s=v,c)$ are the same matrix elements appearing in Eq. (12). Each value of μ in the impulsive excitation model corresponds to a specific optical transition E_{ii}. The k dependence of $S_\mu(k)$ for the RBM phonon in the (11,0) nanotube is shown in Fig. 12 for the first four optical transitions. For the RBM mode, we chose the unit mode polarization vector to point radially outward, so that positive values of $S(k)$ contribute to a radially outward directed driving term.

As can be seen in Fig. 12 both positive and negative values of $S(k)$ are possible. If, for example, we were to pump near the E_{11} band edge, the electron distribution functions would be localized near $k=0$ and we would get negative values for $S(t)$. The signs of the driving function kernels near $k=0$ for the E_{ii} transitions are in agreement with other results reported in the literature.[19] The sign of $S^\beta_\mu(k)$ is the negative of the sign of the electron-phonon matrix element $M^\beta_{c\mu}(k) - M^\beta_{v\mu}(k)$ appearing in Eq. (21). This matrix element has been obtained by Machón *et al.* in an *ab initio* calculation reported in Ref. 19 for the lowest four optical transitions with light polarized parallel to the tube axis. In Table I of Machón *et al.*[19] the sign of the band-edge electron-phonon matrix element for E_{11} in the (11,0) tube has a sign opposite to that of the higher-lying transitions in agreement with the results shown in Fig. 12.

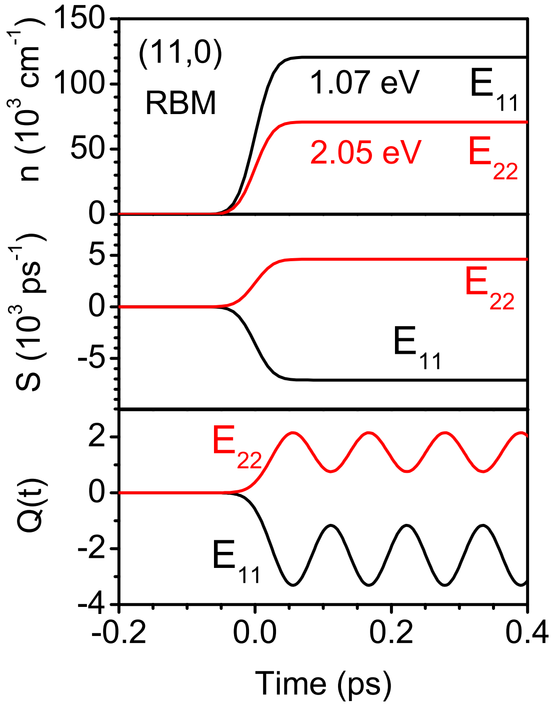

FIG. 13. (Color online) Coherent phonon generation in (11,0) nanotubes by photoexcitation at the E_{11} and E_{22} transition energies. The upper panel shows the density of photoexcited electron-hole pairs per unit length, the middle panel shows the coherent phonon driving function, and the bottom panel shows the RBM coherent phonon amplitude.

In Fig. 13 we plot the photoexcited carrier density $n(t)$, the coherent phonon driving function $S(t)$, and the coherent phonon amplitude $Q(t)$ for RBM coherent phonons in (11,0) tubes for 50 fs z-polarized laser pulses with photoexcitation energies of 1.07 and 2.05 eV. These correspond to the E_{11} and E_{22} absorption peaks seen in Fig. 9, respectively. The absorption peaks are comparable for E_{11} and E_{22}. However, for constant fluence, the number of photoexcited carriers $n \propto \alpha/\hbar\omega$ (see Ref. 42, p. 341) and so the number of photoexcited carriers is larger for the E_{11} transition primarily as a result of the smaller transition energy. As expected from Fig. 12, the coherent phonon driving functions $S(t)$ and amplitudes $Q(t)$ have different signs in the two cases. This means that for photoexcitation at the E_{11} transition in mod 2 nanotubes the tube diameter *decreases* and oscillates about a smaller equilibrium diameter while the opposite is true for photoexcitation at the E_{22} transition energy. As an aside, we note that in mod 1 tubes the predicted E_{22} and E_{11} photoexcited diameter oscillations have the opposite initial phase relative to the corresponding mod 2 oscillations as will be shown in Sec. IV E.

If we pump at the broadened E_{22} absorption peaks with 50 fs pulses of the same spectral width for each nanotube in family 22, we obtain the driving functions shown in the upper panel of Fig. 14. In all cases, the driving functions are positive which implies that all the nanotubes in family 22 initially move radially outward in response to photoexcitation by an ultrafast pump at the E_{22} transition energy. The dimensionless coherent phonon amplitudes $Q(t)$ for the ra-

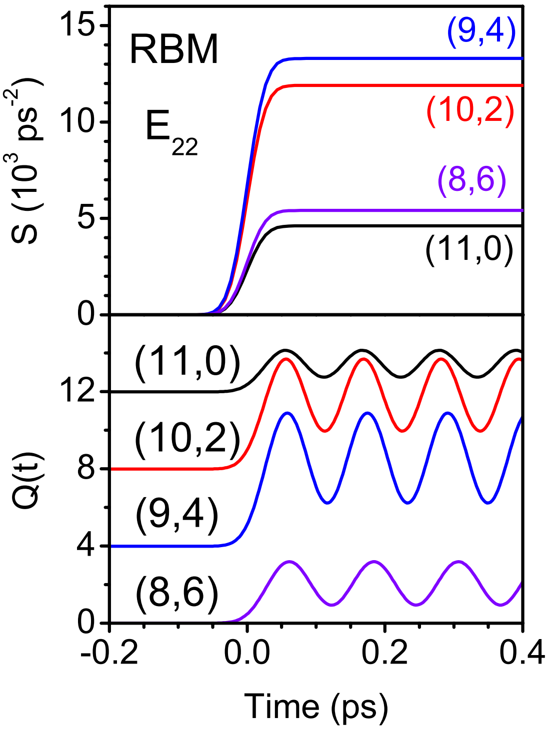

FIG. 14. (Color online) Upper panel: coherent phonon driving functions for RBM oscillations in family 22 nanotubes photoexcited by 50 fs pumps at the broadened E_{22} absorption peaks in Fig. 9. Lower panel: corresponding coherent phonon amplitudes. Curves are offset for clarity.

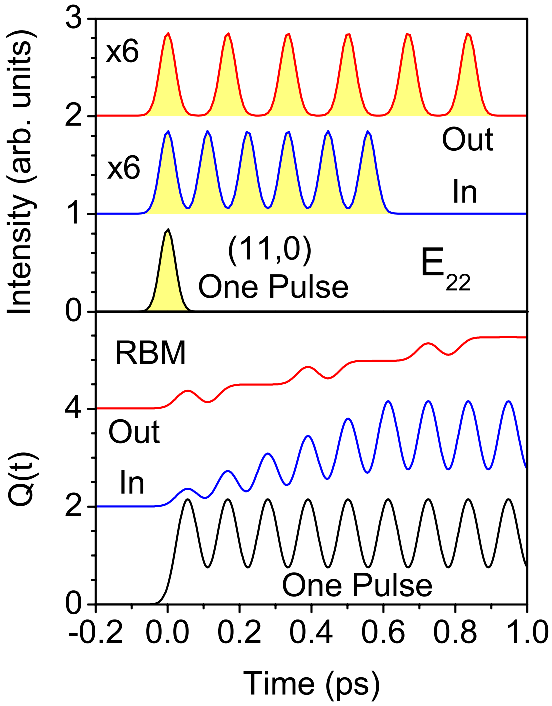

FIG. 15. (Color online) Upper panel: pump laser intensity vs time for a single 50 fs Gaussian pulse and two trains of six 50 fs Gaussian pulses with repetition periods in phase and 180° out of phase with the (11,0) RBM phonon period. In all cases, we pump at the (11,0) E_{22} transition energy (2.05 eV) with the same fluence. Note that the intensities of the two pulse trains are magnified by a factor of 6 relative to the intensity of a single Gaussian pulse. Lower panel: corresponding coherent phonon amplitudes for the (11,0) RBM coherent phonon oscillations.

dial breathing mode obtained by solving the driven oscillator equation (11) are shown in the lower panel of Fig. 14 where the curves are offset for clarity. As expected, the coherent phonon amplitudes oscillate at the RBM frequencies about a new positive equilibrium point. We note that for the radial breathing mode the coherent phonon amplitude is proportional to the differential change in the tube diameter.

In Fig. 14, we see that the magnitude of the coherent phonon oscillations depends on chirality. The size of the jump in the driving function $S(t)$ due to photoexcitation, and therefore the magnitude of the oscillations in $Q(t)$, should be roughly proportional to the product of the electron-photon and electron-phonon matrix elements. The electron-phonon interaction matrix element for E_{22} transitions in mod 2 tubes is largest in the zigzag nanotube limit[18] while the corresponding electron-photon interaction matrix element is largest in the armchair limit.[49] Thus we expect $S(t)$ and $Q(t)$ to have maxima somewhere between these two limits.

C. Resonant excitation of coherent phonons

In our experimental work, we resonantly excite coherent RBM phonons in specific chirality nanotubes in a micelle-suspended sample by using a train of pump pulses with a repetition rate equal to the RBM period. To illustrate resonant excitation of coherent phonons in nanotubes, we repeated our simulations for the (11,0) nanotube using a train of six Gaussian pulses pumping at the E_{22} transition energy (2.05 eV) where the pulse repetition period was in phase and 180° out of phase with the period of the RBM phonon.

The results are illustrated in Fig. 15. The upper panel of Fig. 15 shows the pump laser intensity as a function of time for the in-phase and out-of-phase cases. For comparison, we also plot the pump laser intensity for the single 50 fs Gaussian pulse used in our earlier simulation. In all three cases the fluence is taken to be 10^{-5} J/cm^2 and hence the final density of photogenerated carriers was the same. We note that in the figure, the intensities of the two pulse trains are multiplied by a factor of 6 since the intensities of the Gaussian pulses scale inversely with the number of pulses if the fluence is held constant.

The corresponding coherent phonon amplitudes for the RBM phonons are shown in the lower panel of Fig. 15. For the single Gaussian pulse, the coherent phonon amplitude is the same as that shown in Fig. 14 for the (11,0) nanotube. For the in-phase case, the coherent phonon amplitude is magnified after each Gaussian pulse and at long times is identical to the coherent phonon amplitude obtained using the single Gaussian pulse. Since it is the long-time behavior of the oscillating part of the coherent phonon amplitude that determines the CP signal, the two resulting CP spectra are also identical. When the Gaussian pulses are 180° out of phase, the oscillating part of the coherent phonon amplitude and hence the resulting CP spectra are completely suppressed.

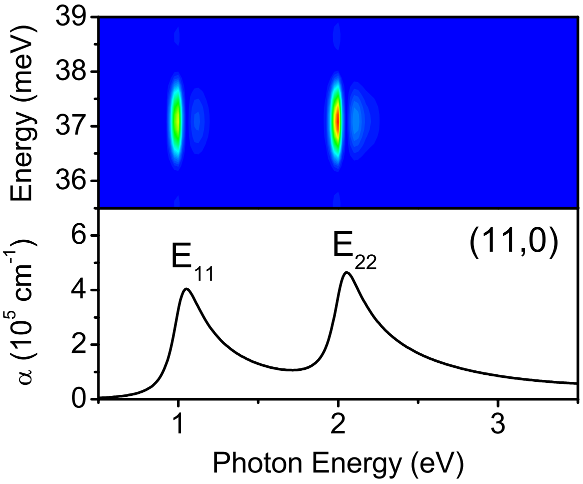

FIG. 16. (Color online) The lower panel shows the absorption coefficient in (11,0) nanotubes as a function of photon energy for light polarized along the tube axis. The upper panel is a contour map showing the coherent phonon power spectrum as a function of pump-probe energy and phonon frequency.

In Fig. 15 the predicted coherent phonon amplitudes at long times oscillate rapidly about the steady-state value $\bar{Q}_\beta = S_\beta(t\rightarrow\infty)/\omega_\beta^2$. In real nanotubes the driving function $S_\beta(t)$ will slowly vanish as the carriers recombine. In addition the coherent phonon amplitudes will slowly decay on a time scale of tens of picoseconds as evidenced in Fig. 3.

D. Coherent phonon detection in mod 2 tubes

The generation of coherent phonons results in periodic oscillations of the carbon atoms which in turn modulate the optical properties of the nanotube. These coherent phonon oscillations can be detected by measuring transient optical properties in pump-probe experiments. We simulate single-color pump-probe measurements in which we pump with light linearly polarized along the tube axis and measure the transient differential gain as a function of probe delay for a probe pulse having the same energy and polarization as the pump. The coherent phonon spectrum is obtained by scanning the pump-probe energy and, in our simulations, the pump fluence, the duration, and the FWHM spectral linewidth are assumed to be constant as we vary the pump-probe energy.

The coherent phonon (CP) spectrum for mod 2 (11,0) nanotubes is shown in Fig. 16. The bottom panel shows the absorption spectrum for light linearly polarized along the tube axis assuming a FWHM linewidth of 0.15 eV. The upper panel shows a contour map of the coherent phonon power spectrum as a function of pump-probe energy and photon energy. The CP intensity is proportional to the power spectrum and as we scan in photon energy two large peaks are observed at the E_{11} and E_{22} transitions at a phonon energy near 37.1 meV (300 cm^{-1}) which corresponds to the RBM frequency of the (11,0) nanotube. Comparing the upper and lower panels of Fig. 16, we can verify our earlier assertion that as we scan in pump energy the CP intensity at the RBM coherent phonon frequency is proportional to the absolute value of the first derivative of the absorption coefficient. We should point out that our theoretical model does not include many-body Coulomb effects and so the position and the shape of the CP signal are due to modulation of the free carrier E_{11} and E_{22} transitions. Thus in our free carrier model, we see an asymmetric double peak at each transition with the stronger peak at low pump energy and the weaker peak at higher energy.

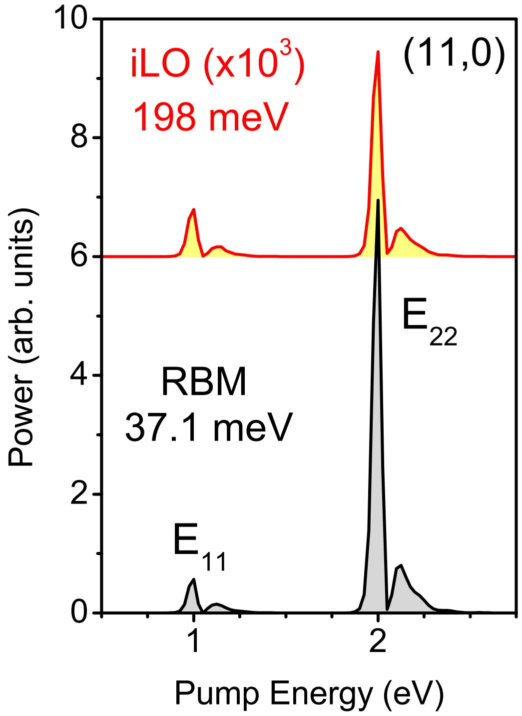

FIG. 17. (Color online) Coherent phonon spectra for coherent RBM and LO phonons in (11,0) nanotubes photoexcited by an ultrafast *z*-polarized 5 fs pump. The CP spectra at the RBM and LO energies (37.1 and 198 meV) are plotted as a function of pump-probe energy. Two features are seen near E_{11} and E_{22} transitions. The LO curve is multiplied by 1000 and offset for clarity.

In our simulations with 50 fs laser pulses, we excite coherent RBM phonon modes since the pulse duration is much less than the RBM phonon oscillation period. To excite the higher-lying coherent phonon modes, it is necessary to use shorter laser pulses. Recently, Gambetta *et al.*[11] used sub-10-fs laser pulses to excite the RBM and LO modes while excitation of the oTO and iTO modes were not observed. To examine this case, we simulated CP spectroscopy in (11,0) nanotubes using short 5 fs laser pulses. In qualitative agreement with the measurements of Gambetta *et al.*, we find that the two strongest modes are the RBM and LO modes, while the strengths of the oTO and iTO modes are found to be negligible. Our result for the iTO mode is consistent with the chirality-dependent Raman *G*-band intensity in which the iTO signal is absent in zigzag nanotubes.[50] The CP spectra for the RBM and LO modes are shown in Fig. 17 where the differential gain power spectra at the RBM and LO energies (37.1 and 198 meV, respectively) are plotted as a function of pump-probe energy. Two strong features are seen near the E_{11} and E_{22} transition energies. In this example, the two curves have similar shapes but the LO CP spectrum (multi-

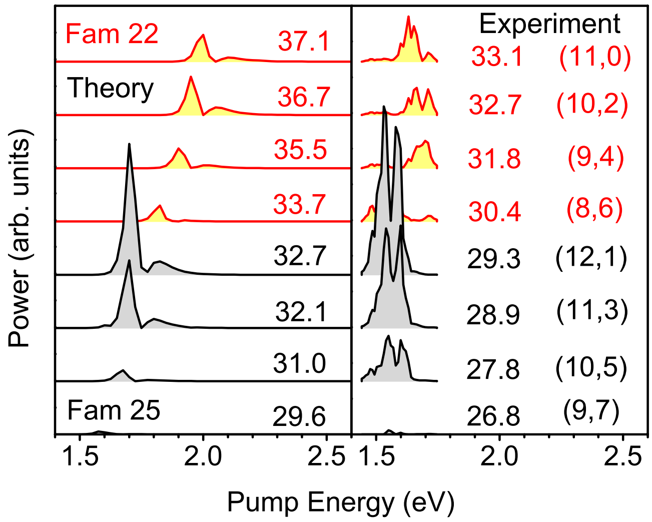

FIG. 18. (Color online) Coherent phonon intensity at the RBM frequency as a function of pump-probe energy for several mod 2 semiconducting nanotubes at the E_{22} transition. The experimental CP spectra are in the right panel and the simulated CP spectra are in the left panel. The upper four curves in each panel are for nanotubes in family 22 and the lower four curves are for tubes in family 25. Each curve is labeled with the chirality (n,m) and the RBM phonon energy in meV and offset for clarity.

plied by a factor of 1000 in the figure) is much weaker than the corresponding RBM spectrum. We note that shortening the duration of the laser pulse from 50 to 5 fs enhances the strength of the E_{22} peak relative to the E_{11} peak. This can best be seen by comparing the bottom curves in Fig. 17 with the bottom curve in Fig. 21.

It is useful to examine trends in the CP spectra within and between mod 2 semiconducting nanotube families by plotting the theoretical CP intensity at the RBM phonon frequency as a function of pump-probe energy. This is done in the left panel of Fig. 18 where we plot our theoretical CP intensity at the RBM frequency as a function of pump-probe energy for all nanotubes in families 22 and 25. The curves for each nanotube are labeled with the nanotube chirality (n,m) and the RBM phonon energy in meV. In each nanotube, we see peaks in the CP spectra corresponding to E_{22} transitions. Within a given family, the CP intensity tends to decrease as the chiral angle increases, i.e., as the chirality goes from $(n,0)$ zigzag tubes to (n,n) armchair tubes. From Fig. 18 we can also see that the theoretical CP intensity increases as we go from family 22 to family 25.

The right panel of Fig. 18 shows the corresponding experimental CP spectra for the nanotubes in families 22 and 25. Comparing experimental and theoretical curves in Fig. 18, we see that our theory correctly predicts the overall trends in the CP intensities. Since we are using pump-probe methods to study an ensemble of micelle-suspended nanotubes, the relative agreement between the theoretically calculated and experimentally measured CP intensities suggests that nanotubes of different chiralities in families 22 and 25 in the micelle-suspended sample studied are equally probable and that the measured CP signal strengths are an intrinsic property of the tubes.

There are discrepancies in the predicted pump-probe energies of the peaks on the order of 0.4 eV or less. A discrepancy of this size is expected since we have not included many-body Coulomb interactions in our theoretical model. It is well established that both the excitonic redshift and the self-energy blueshift are very large in nanotubes, with the latter exceeding the former.[9,51–55] We also note that the dielectric function of the surrounding medium also influences the excitonic transition energies.[56] There are also differences between the theoretical and experimental CP line shapes in Fig. 18. If we compare theoretical and experimental CP spectra for the (12,1) nanotube, we see that both exhibit a double peaked structure. However, the lower-energy theoretical peak is much stronger than the higher-energy peak whereas the two experimental peaks have comparable strength. This discrepancy can be attributed to strong excitonic modification of the shape of the nanotube absorption spectrum whose time-dependent modulation of the probe pulse gives rise to the shape of the CP signal. The free carrier absorption edge is highly asymmetric while the excitonic absorption spectrum exhibits a symmetric peak at the exciton transition energy, thus accounting for the discrepancy. Our theory qualitatively agrees with experiment; but to obtain quantitative agreement, one must include details of the Coulomb interaction.

Our experimental and theoretical results are also in qualitative agreement with the results of CP spectroscopy measurements previously reported by Lim *et al.* in Ref. 12. As these authors note, the tendency of the CP intensity to increase with family index is in contrast to the situation in resonant Raman scattering where the strength of the resonant Raman signal is observed to decrease as the family index increases.

E. Coherent phonon detection in mod 1 tubes

It is useful to perform a comparison between mod 1 and mod 2 semiconducting nanotubes with the same chiral angle. To this end, we compare the family 22 (11,0) mod 2 nanotubes with family 26 (13,0) mod 1 tubes. In both cases, the pump lasers have the same fluence (10^{-5} J/cm^2), pulse duration (50 fs), and spectral linewidth (0.15 eV); while the pump energies correspond to the maxima in the broadened E_{22} absorption features. For the (11,0) tube we pump at 2.05 eV and for the (13,0) tube we pump at 1.84 eV. The time-dependent photogenerated carrier densities per unit length are shown in the upper panel of Fig. 19. The middle and lower panels show the coherent phonon driving functions and the corresponding coherent phonon amplitudes for RBM coherent phonons in the two cases. For (11,0) mod 2 tubes, the coherent phonon driving function is *positive* while for (13,0) mod 1 tubes, the driving function is found to be *negative*.

Some insight into this behavior can be obtained by examining the k-dependent driving function kernel for coherent RBM phonons in (13,0) nanotubes shown in Fig. 20. Comparing Fig. 20 with Fig. 12, we see that the driving function kernels for E_{11} and E_{22} transitions near $k=0$ have opposite signs which accounts for the sign change.

These results are supported by other studies reported in the literature.[18] The difference in the sign of the E_{22} driving

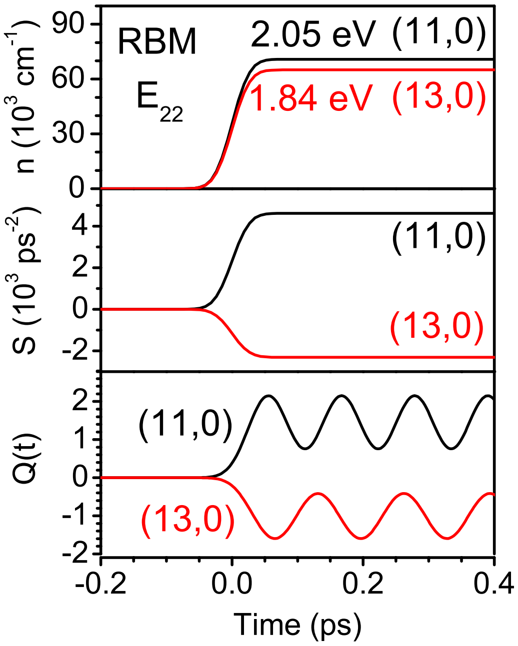

FIG. 19. (Color online) Coherent phonon generation in (11,0) mod 2 and (13,0) mod 1 semiconducting zigzag nanotubes by photoexcitation at the E_{22} transition energy. The upper panel shows the density of photoexcited electron-hole pairs per unit length, the middle panel shows the coherent phonon driving function, and the bottom panel shows the RBM coherent phonon amplitude.

function kernels at $k=0$ for the zigzag mod 2 (11,0) tube shown in Fig. 12 and the zigzag mod 1 (13,0) tube shown in Fig. 20 is due to a change in sign of the electron-phonon matrix element. This sign change in the electron-phonon matrix element for tubes with different mod numbers was also obtained independently by Jiang *et al.* in Ref. 18. Figure 1(a) of Jiang *et al.*[18] shows the electron-phonon matrix element for coherent RBM phonons excited at the E_{22} transition as a function of the chiral angle θ for mod 1 and mod 2 tubes [the SII and SI curves in Fig. 1(a) of Jiang *et al.*]. For zigzag tubes, $\theta=0$ and from Fig. 1(a) of Jiang *et al.* we can see that the sign of the electron-phonon matrix element for the mod 2 (SI) tube is positive while the sign of the electron-phonon matrix element for the mod 1 (SII) tube is negative. This is consistent with the theoretical results shown in Figs. 12 and 20.

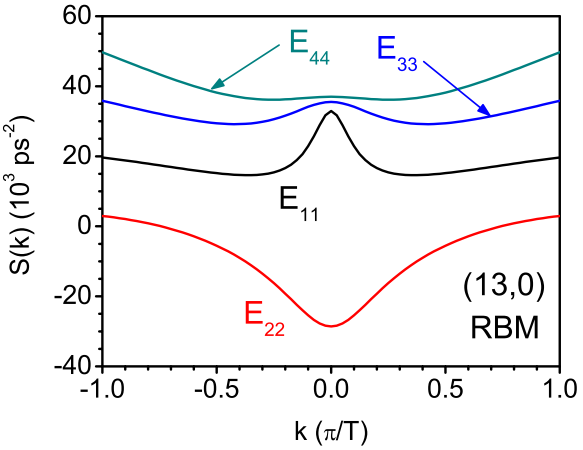

FIG. 20. (Color online) Driving function kernel for RBM coherent phonons in the (13,0) nanotube for several optical transitions E_{ii} in the impulsive excitation approximation.

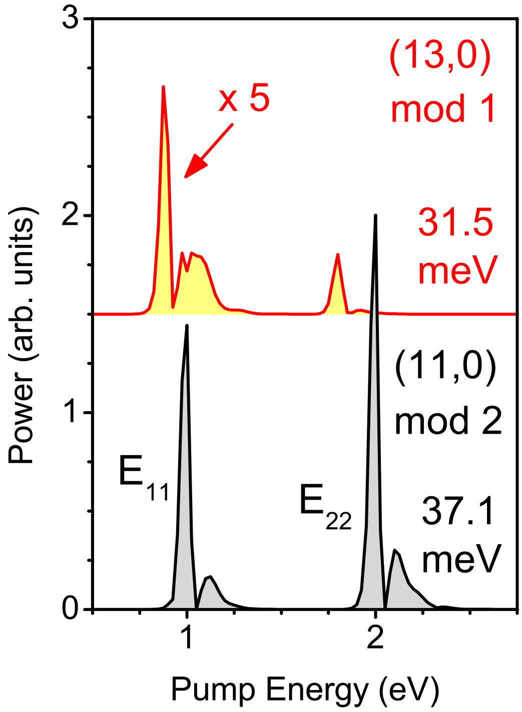

FIG. 21. (Color online) Coherent phonon power spectra at the RBM energies in the (13,0) mod 1 and (11,0) mod 2 semiconducting nanotubes as a function of pump-probe energy. The mod 1 CP power spectrum is multiplied by a factor of 5 and offset for clarity.

We find that the CP intensity is very sensitive to the nanotube mod number. In general, the CP intensity in mod 2 semiconducting nanotubes is much larger than the CP intensity in mod 1 semiconducting tubes. This is illustrated in Fig. 21 where we plot the CP power spectra as a function of pump-probe energy at the RBM frequencies for the zigzag (13,0) mod 1 and (11,0) mod 2 semiconducting nanotubes. For the (13,0) and (11,0) tubes the RBM phonon energies are 31.5 (254 cm^{-1}) and 37.1 meV (300 cm^{-1}), respectively. Note that in Fig. 21 the mod 1 curve is multiplied by a factor of 5. In general, we find that CP intensities in mod 2 tubes are considerably larger than CP intensities in mod 1 tubes. This is consistent with the experimental results of Lim *et al.* as reported in Refs. 12 and 13. We also find that, in mod 1 tubes, the E_{11} feature is more pronounced than the E_{22} feature in contrast to what is seen in the mod 2 case.

The CP intensities as a function of chirality for nanotubes in two mod 1 families (families 26 and 29) are shown in Fig. 22. We find that in all cases the E_{11} features in the mod 1 tubes are much stronger than the E_{22} features. Within a mod 1 family, the CP intensity of the E_{11} feature is found to decrease with increasing chiral angle. We also find that the CP intensities decrease as the mod 1 family index increases.

V. SUMMARY

Using femtosecond pump-probe spectroscopy with pulse-shaping techniques, we have generated and detected coherent

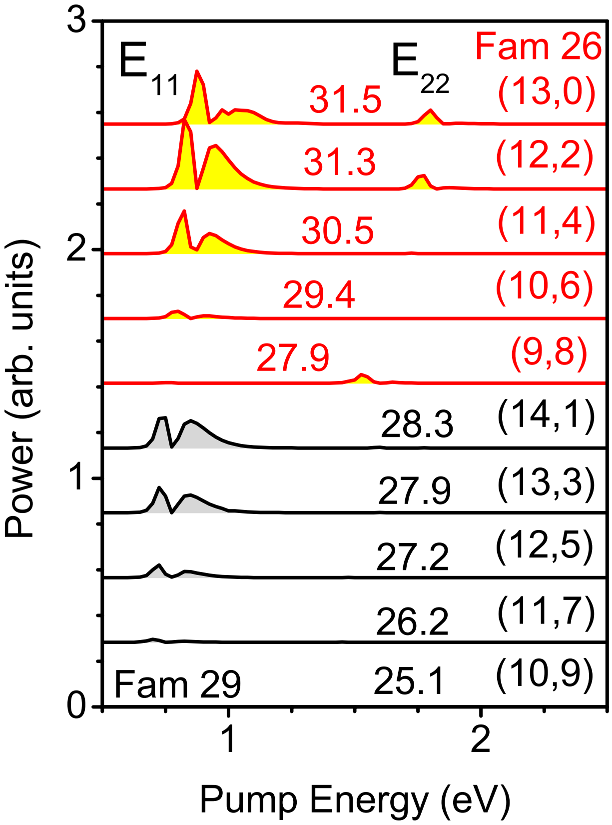

FIG. 22. (Color online) Coherent phonon intensity at the RBM frequency as a function of pump-probe energy for several mod 1 semiconducting nanotubes. The upper five curves are for nanotubes in family 26 and the lower five curves are for tubes in family 29. Each curve is labeled with the chirality (n,m) and the RBM phonon energy in meV. The curves are offset for clarity.

phonons in chirality-specific semiconducting single-walled carbon nanotubes. The signals were resonantly enhanced when the pump photon energy coincides with an interband exciton resonance, and the analysis of such data provided a wealth of information on the chirality dependence of light absorption, phonon generation, and phonon-induced band-structure modulations.

To explain our experimental results qualitatively and quantitatively, we have developed a microscopic theory for the generation and detection of coherent phonons in semiconducting single-walled carbon nanotubes via coherent phonon spectroscopy. For extremely short laser pulses, we find that the two strongest coherent phonon modes are the RBM and LO modes. The CP spectrum of the LO mode is similar in shape to that of the RBM mode but is found to be much weaker.

For the RBM modes, the CP intensity within a mod 2 family tends to decrease with chiral angle, and the decrease in CP intensity with chiral angle is found to be much more pronounced for the E_{11} feature. We also find that CP intensities are considerably weaker in mod 1 families in comparison with mod 2 families. In general, the E_{22} CP intensities in mod 2 families are stronger than the E_{11} features. For RBM modes in mod 1 tubes, the E_{11} intensities are stronger than the E_{22} intensities and tend to decrease with increasing chiral angle within a given family. As the family index increases, the E_{11} CP intensity in mod 1 tubes decreases.

For mod 2 nanotubes, we predict that the tube diameter will initially increase for E_{22} photoexcitation and decrease for E_{11} photoexcitation. In mod 1 nanotubes, the opposite is predicted to be the case, i.e., the tube diameter will initially decrease for E_{22} photoexcitation and increase for E_{11} photoexcitation.

We compare our theoretical results with experimental CP spectra in mod 2 nanotubes and find that our theoretical model correctly predicts the overall trends in the relative strengths of the CP signal both within and between mod 2 families. We find discrepancies between our theoretical predictions with regard to the peak positions and line shapes, which we attribute to Coulomb interaction effects that are not included in our calculations.

For (11,3) mod 2 nanotubes, we experimentally verified our theoretical prediction that the diameter of E_{22} photoexcited nanotubes initially increases. However, we were unable to get a good sample for verifying our related prediction that the diameter of E_{22} photoexcited mod 1 nanotubes initially decreases. This will be one of the goals of our future studies.

ACKNOWLEDGMENTS

This work was supported by the National Science Foundation under Grants No. DMR-0325474, No. OISE-0530220, and No. DMR-0706313 and by the Robert A. Welch Foundation under Grant No. C-1509. Y.-S.L. and K.-J.Y. are supported by a Korea Science and Engineering Foundation (KOSEF) grant funded by the Korean Government (MOST) (Grant No. R01-2007-000-20651-0). R.S. is supported by the Ministry of Education, Culture, Sports, Science and Technology-Japan (MEXT) under Grants No. 16076201 and No. 20241023.

APPENDIX A: ELECTRONIC STATES

The tight-binding wave functions for the electronic states in carbon nanotubes are expanded in terms of the symmetry-adapted basis functions,

$$|k,\mu\rangle = \sum_{r} C_r(k,\mu)|k,\mu,r\rangle, \tag{A1}$$

where $r=A,B$ labels the atoms in the two-atom unit cell, $C_r(k,\mu)$ are expansion coefficients, and $|k,\mu,r\rangle$ are symmetry-adapted basis functions. The symmetry-adapted basis functions are linear combinations of localized atomic π orbitals,

$$|k,\mu,r\rangle = \frac{1}{\sqrt{N}}\sum_{\mathbf{J}} e^{i\hat{\mathbf{k}}(k,\mu)\cdot\mathbf{R}_{\mathbf{J}}}|\mathbf{J},r\rangle, \tag{A2}$$

where N is the number of two-atom unit cells in the system and $|\mathbf{J},r\rangle$ is a localized atomic π orbital on atom r in the two-atom unit cell at $\mathbf{R}_{\mathbf{J}}$. The positions of the two-atom unit cells (in unrolled graphene xy coordinates) are

$$\mathbf{R}_{\mathbf{J}} = j_1\mathbf{a}_1 + j_2\mathbf{a}_2, \tag{A3}$$

where $\mathbf{J}=(j_1,j_2)$ and $\mathbf{a}_1=(\frac{\sqrt{3}a}{2},\frac{a}{2})$ and $\mathbf{a}_2=(\frac{\sqrt{3}a}{2},-\frac{a}{2})$ are the graphene basis vectors.

The two-dimensional wave vector $\hat{\mathbf{k}}(k,\mu)$ appearing in the symmetry-adapted basis function expansion in Eq. (A2) is determined by imposing translational and rotational boundary conditions on the nanotube. Imposing the translational boundary condition, we have

$$\hat{\mathbf{k}}(k,\mu)\cdot\mathbf{T}=kT, \tag{A4}$$

where $\mathbf{T}=t_1\mathbf{a}_1+t_2\mathbf{a}_2$ is the nanotube translational vector which is parallel to the tube axis and has the length of the translational unit cell. Explicit expressions for t_1 and t_2 in terms of the chiral indices n and m can be found in Ref. 1 and are given by $t_1=\frac{2m+n}{d_R}$ and $t_2=-\frac{2n+m}{d_R}$, where $d_R=\gcd(2n+m,2m+n)$. The rotational boundary condition is

$$\hat{\mathbf{k}}(k,\mu)\cdot\mathbf{C}_h=2\pi\mu, \tag{A5}$$

where $\mathbf{C}_h=n\mathbf{a}_1+m\mathbf{a}_2$ is the chiral vector in unrolled graphene coordinates and $\mu=0,\ldots,N_{\text{hex}}-1$ is an angular-momentum quantum number that labels the cutting lines in the simple zone folding picture.[1]

From Eqs. (A1)–(A5), we arrive at the symmetry-adapted tight-binding wave function,

$$|k,\mu\rangle=\frac{1}{\sqrt{N}}\sum_{r,\mathbf{J}}e^{i\phi_{\mathbf{J}}(k,\mu)}|\mathbf{J},r\rangle \tag{A6}$$

with the phase factor $\phi_{\mathbf{J}}(k,\mu)\equiv\hat{\mathbf{k}}(k,\mu)\cdot\mathbf{R}_{\mathbf{J}}$ given by

$$\phi_{\mathbf{J}}(k,\mu)=\frac{\pi\mu[(2n+m)j_1+(2m+n)j_2])}{n^2+nm+m^2}+\frac{\sqrt{3}ak}{2}\frac{mj_1-nj_2}{\sqrt{n^2+nm+m^2}}. \tag{A7}$$

Substituting the symmetry-adapted tight-binding wave function (A6) into the Schrödinger equation, we obtain, for each value of μ, a 2×2 matrix eigenvalue equation for the electronic energies $E_{s\mu}(k)$ and the expansion coefficients $C_r(s,\mu,k)$, namely,

$$\sum_{r'}H_{r,r'}C_{r'}=E_{s\mu}(k)\sum_{r'}S_{r,r'}C_{r'}, \tag{A8}$$

where $s=v,c$ labels the valence- and conduction-band states. The 2×2 Hamiltonian and overlap matrices are given by

$$H_{r,r'}=\sum_{\mathbf{J}'}e^{i\phi_{\mathbf{J}'}(k,\mu)}\langle0,r|H|\mathbf{J}',r'\rangle \tag{A9}$$

and

$$S_{r,r'}=\sum_{\mathbf{J}'}e^{i\phi_{\mathbf{J}'}(k,\mu)}\langle0,r|\mathbf{J}',r'\rangle. \tag{A10}$$

In the sum over $\mathbf{J}'=(j_1',j_2')$, in Eqs. (A9) and (A10) we keep only the on-site and third nearest-neighbor contributions since the parameterized matrix elements vanish at distances beyond the third nearest-neighbor distance in graphene. Values of (j_1,j_2) for the first to fourth nearest neighbors of the A and B atoms in the two-atom unit cell $\mathbf{J}=(0,0)$ are easy to work out and can be found in Table 2 of Ref. 57.

APPENDIX B: PHONON MODES

Here we derive the block diagonal 6×6 dynamical matrices and symmetry-adapted atomic displacement vectors for phonon modes in a carbon nanotube. The equilibrium position of the rth atom in the Jth unit cell is $\mathbf{R}_{r\mathbf{J}}=\mathbf{R}_{\mathbf{J}}+\tau_r$, where $\tau_A=(-\frac{a}{2\sqrt{3}},0)$ and $\tau_B=(\frac{a}{2\sqrt{3}},0)$. The position of the two-atom unit cell in unrolled graphene xy coordinates, $\mathbf{R}_{\mathbf{J}}$, is defined by Eq. (A3) in Appendix A. The positions of the nearest-neighbor atoms are $\mathbf{R}_{r\mathbf{J}}^{\alpha l}$, where α denotes the nearest-neighbor shell and l labels the atoms within the αth shell. The corresponding instantaneous atomic displacements are $\mathbf{U}_{r\mathbf{J}}$ and $\mathbf{U}_{r\mathbf{J}}^{\alpha l}$. In this notation the bond stretching potential is given by[31]

$$V_s=\sum_{r\mathbf{J},\alpha l}\frac{\Gamma_s^{\alpha}}{2}[\hat{\mathbf{n}}_{r\mathbf{J}}^{\alpha l}\cdot(\mathbf{U}_{r\mathbf{J}}^{\alpha l}-\mathbf{U}_{r\mathbf{J}})]^2, \tag{B1}$$

where $\hat{\mathbf{n}}_{r\mathbf{J}}^{\alpha l}$ is a unit vector parallel to $\mathbf{R}_{r\mathbf{J}}^{\alpha l}-\mathbf{R}_{r\mathbf{J}}$ and Γ_s^{α} are the bond stretching force constants.

The nearest-neighbor in-plane bond bending potential is given by[32]

$$V_{bb}=\sum_{r\mathbf{J}}\sum_{ll'}{}'\frac{\Gamma_{bb}}{2}[\hat{\mathbf{n}}_{r\mathbf{J}}^{1l}\cdot(\mathbf{U}_{r\mathbf{J}}^{1l'}-\mathbf{U}_{r\mathbf{J}})+\hat{\mathbf{n}}_{r\mathbf{J}}^{1l'}\cdot(\mathbf{U}_{r\mathbf{J}}^{1l}-\mathbf{U}_{r\mathbf{J}})]^2 \tag{B2}$$

where Γ_{bb} is the in-plane bond bending force constant. The prime on the sum over nearest neighbors l and l' indicates that the $l=l'$ term is omitted. The out-of-surface bond bending potential is given by[31]

$$V_{rb}=\sum_{r\mathbf{J}}\frac{\Gamma_{rb}}{2}\left[\sum_{l}\hat{\varrho}_{r\mathbf{J}}\cdot(\mathbf{U}_{r\mathbf{J}}^{1l}-\mathbf{U}_{r\mathbf{J}})\right]^2, \tag{B3}$$

where Γ_{rb} is the out-of-plane bond bending force constant. The unit vector $\hat{\varrho}_{r\mathbf{J}}$ is given by

$$\hat{\varrho}_{r\mathbf{J}}=\frac{\sum_{l}[\mathbf{R}_{r\mathbf{J}}^{1l}-\hat{\mathbf{z}}(\hat{\mathbf{z}}\cdot\mathbf{R}_{r\mathbf{J}})]}{\left|\sum_{l}[\mathbf{R}_{r\mathbf{J}}^{1l}-\hat{\mathbf{z}}(\hat{\mathbf{z}}\cdot\mathbf{R}_{r\mathbf{J}})]\right|} \tag{B4}$$

and for large diameter nanotubes is approximately equal to the radial outward unit vector at $\mathbf{R}_{r\mathbf{J}}$. As pointed out in Ref. 31 the form of $\hat{\varrho}_{r\mathbf{J}}$ in Eq. (B4) is required to preserve rigid rotational invariance.

The bond twisting potential is given by[31]

$$V_{\text{tw}}=\sum_{\langle i,j\rangle}\frac{\Gamma_{\text{tw}}}{2}\{\hat{\mathbf{r}}_{\langle i,j\rangle}\cdot[(\mathbf{U}_1+\mathbf{U}_2)-(\mathbf{U}_3+\mathbf{U}_4)]\}^2, \tag{B5}$$

where Γ_{tw} is the bond twisting force constant. In the sum $\langle i,j\rangle$ represents a bond between atom i and one of its nearest neighbors j and $\hat{\mathbf{r}}_{\langle i,j\rangle}$ is the radially outward unit vector at the midpoint of the bond. The atomic displacements $\mathbf{U}_1,\ldots,\mathbf{U}_4$ are the displacements of the four atoms attached to the $\langle i,j\rangle$ bond with $\mathbf{U}_1$ related to $\mathbf{U}_2$ by a C_2 rotation about $\hat{\mathbf{r}}_{\langle i,j\rangle}$. The equations of motion for the carbon atoms are

$$M\frac{\partial^2 \mathbf{U}_{r\mathbf{J}}}{\partial t^2} = -\frac{\partial V}{\partial \mathbf{U}_{r\mathbf{J}}}, \tag{B6}$$

where M is the mass of a carbon atom and $V = V_s + V_{bb} + V_{rb} + V_{\text{tw}}$ is the ionic vibrational potential.

Symmetry-adapted atomic displacement vectors, for each value of ν, can be written as

$$\mathbf{U}_{r\mathbf{J}} = S(\theta_{\mathbf{J}})\hat{\mathbf{e}}_r(q,\nu)e^{i[\phi_{\mathbf{J}}(q,\nu)+\omega t]}, \tag{B7}$$

where q is the phonon wave vector, $\nu = 0,\ldots,N_{\text{hex}}-1$ labels the cutting lines, and ω is the phonon frequency. The unit vector $\hat{\mathbf{e}}_r(q,\nu)$ is the phonon mode polarization for the rth atom in the $\mathbf{J}=(0,0)$ two-atom unit cell. The phase factor $\phi_{\mathbf{J}}(q,\nu)$ is obtained from Eq. (A7) by replacing k,μ with q,ν.

The matrix $S(\theta_{\mathbf{J}})$ is a unitary rotation matrix for rotations about the nanotube axis (taken to be z) and it acts to rotate $\hat{\mathbf{e}}_r(q,\nu)$ to the $\mathbf{J}$th two-atom unit cell. The counterclockwise rotation angle is $\theta_{\mathbf{J}} = j_1\theta_1 + j_2\theta_2$, where

$$\theta_1 = \frac{(2n+m)\pi}{n^2+nm+m^2} \tag{B8}$$

and

$$\theta_2 = \frac{(2m+n)\pi}{n^2+nm+m^2}. \tag{B9}$$

Substituting the atomic displacement vectors (B7) into the equations of motion (B6), we obtain an eigenvalue problem for the phonon frequencies and mode polarization vectors,

$$\sum_{r'} \mathbf{D}_{r,r'}(q,\nu)\hat{\mathbf{e}}_r(\beta,q,\nu) = M\omega^2_{\beta\nu}(q)\hat{\mathbf{e}}_r(\beta,q,\nu), \tag{B10}$$

where $\mathbf{D}_{r,r'}(q,\nu)$ is a 6×6 dynamical matrix for each value of ν and $\omega_{\beta\nu}(q)$ is the phonon-dispersion relation with $\beta = 1,\ldots,6$. Explicit expressions for the symmetry-adapted 6×6 dynamical matrix in terms of the atomic force constants can be found in Refs. 57 and 58. The force constants obtained from the fit shown in Fig. 7 are $\Gamma_s^1 = 237.6$, $\Gamma_s^2 = 17.47$, $\Gamma_s^3 = 2.895$, $\Gamma_s^4 = 7.166$, $\Gamma_{bb} = 18.37$, $\Gamma_{rb} = 16.67$, and $\Gamma_{\text{tw}} = 6.609$ in units of J/m^2.

APPENDIX C: ELECTRON-PHONON INTERACTION MATRIX ELEMENTS

The electron-phonon interaction matrix element in Eq. (8) is given by

$$M^{\mu,\nu}_{s,s',\beta}(k,q) = -A_{\beta,\nu}(q)\sum_{r''}\hat{\mathbf{e}}_{r''}(\beta,q,\nu)\cdot\sum_{r'\mathbf{J}'}C^*_{r'}(s',\mu+\nu,k+q)e^{-i\phi_{\mathbf{J}'}(k+q,\mu+\nu)} \times \sum_{r\mathbf{J}} C_r(s,\mu,k)e^{i\phi_{\mathbf{J}}(k,\mu)}\vec{\lambda}(r'\mathbf{J}',r'',r\mathbf{J}), \tag{C1}$$

where $C_r(s,\mu,k)$ are the electronic expansion coefficients in Eq. (A8), $\phi_{\mathbf{J}}(k,\mu)$ is the phase function defined in Eq. (A7), and $\hat{\mathbf{e}}_r(\beta,q,\nu)$ are the phonon polarization vectors in Eq. (B10). In Eq. (C1), we choose $\mathbf{J}''=0$, so that $S(\theta_{\mathbf{J}''})=1$ and restrict sums over $r\mathbf{J}$ and $r'\mathbf{J}'$ to fourth nearest neighbors of $\mathbf{R}_{r'',0}$. The deformation potential vectors $\vec{\lambda}(r'\mathbf{J}',r'',r\mathbf{J})$ appearing in Eq. (C1) are three-center integrals defined as

$$\vec{\lambda} = \int d\mathbf{r}\ \varphi^*_{r'\mathbf{J}'}(\mathbf{r}-\mathbf{R}_{r'\mathbf{J}'})\,\nabla v_c(\mathbf{r}-\mathbf{R}_{r''0})\varphi_{r\mathbf{J}}(\mathbf{r}-\mathbf{R}_{r\mathbf{J}}), \tag{C2}$$

where $\varphi_{r\mathbf{J}}(\mathbf{r}-\mathbf{R}_{r\mathbf{J}})$ is a π orbital $|r\mathbf{J}\rangle$ localized at $\mathbf{R}_{r\mathbf{J}}$ and $v_c(\mathbf{r}-\mathbf{R}_{r''0})$ is a carbon atom potential centered at $\mathbf{R}_{r''0}$.

We evaluate the deformation potential vectors $\vec{\lambda}$ using the $2p_z$ atomic wave functions and the screened atomic potential for carbon in Ref. 18 obtained from an *ab initio* calculation in graphene.[59] The π orbitals at $\mathbf{R}_{r\mathbf{J}}$ are

$$\varphi_{r\mathbf{J}}(\mathbf{r}) = (\mathbf{r}\cdot\hat{\rho}_{r\mathbf{J}})\sum_l I_l \exp\left(-\frac{r^2}{2\sigma_l^2}\right), \tag{C3}$$

where $\hat{\rho}_{r\mathbf{J}}$ is a unit vector normal to the surface of the nanotube at $\mathbf{R}_{r\mathbf{J}}$. Using Eq. (C3) for the π orbitals in the evaluation of $\vec{\lambda}$ allows us to take the relative orientation of the π orbitals on different sites into account. Similarly the atomic potentials are taken to be

$$v_c(\mathbf{r}) = \frac{1}{r}\sum_l v_l \exp\left(-\frac{r^2}{2\tau_l^2}\right). \tag{C4}$$

Values of I_l, v_l, σ_l and τ_l are tabulated in Table I of Ref. 18. Substituting expansions (C3) and (C4) into Eq. (C2) we obtain an expansion for $\vec{\lambda}$ in terms of three-dimensional integrals. In the case of graphene, the three-dimensional integrals can be done analytically.[18,59] For the nanotube case we can reduce the three-dimensional integrals to one-dimensional integrals that can be done numerically.

---

[1] R. Saito, G. Dresselhaus, and M. Dresselhaus, *Physical Properties of Carbon Nanotubes* (World Scientific, Singapore, 2003).

[2] M. Dresselhaus, *Carbon Nanotubes: Synthesis, Structure, Properties, and Applications* (Springer, New York, 2001).

[3] P. Harris, *Carbon Nanotubes and Related Structures: New Materials for the Twenty-First Century* (Cambridge University Press, Cambridge, England, 1999).

[4] J.-C. Charlier, X. Blase, and S. Roche, Rev. Mod. Phys. **79**, 677 (2007).

[5] M. Terrones, Annu. Rev. Mater. Sci. **33**, 419 (2003).

[6] A. Jorio, R. Saito, J. H. Hafner, C. M. Lieber, M. Hunter, T. McClure, G. Dresselhaus, and M. S. Dresselhaus, Phys. Rev. Lett. **86**, 1118 (2001).

[7] A. Jorio, M. Pimenta, A. Filho, R. Saito, G. Dresselhaus, and M. Dresselhaus, New J. Phys. **5**, 139 (2003).

[8] S. K. Doorn, D. A. Heller, P. W. Barone, M. L. Usrey, and M. S. Strano, Appl. Phys. A: Mater. Sci. Process. **78**, 1147 (2004).

[9] J. Jiang, R. Saito, G. G. Samsonidze, A. Jorio, S. G. Chou, G. Dresselhaus, and M. S. Dresselhaus, Phys. Rev. B **75**, 035407 (2007).

[10] J. Jiang, R. Saito, K. Sato, J. S. Park, G. G. Samsonidze, A. Jorio, G. Dresselhaus, and M. S. Dresselhaus, Phys. Rev. B **75**, 035405 (2007).
[11] A. Gambetta, C. Manzoni, E. Menna, M. Meneghetti, G. Cerullo, G. Lanzani, S. Tretiak, A. Piryatinski, A. Saxena, R. L. Martin, and A. R. Bishop, Nat. Phys. **2**, 515 (2006).
[12] Y.-S. Lim, K.-J. Yee, J. H. Kim, E. H. Hároz, J. Shaver, J. Kono, S. K. Doorn, R. H. Hauge, and R. E. Smalley, Nano Lett. **6**, 2696 (2006).
[13] Y.-S. Lim, K.-J. Yee, J. H. Kim, E. H. Hároz, J. Shaver, J. Kono, S. K. Doorn, R. H. Hauge, and R. E. Smalley, J. Korean Phys. Soc. **51**, 306 (2007).
[14] K. Kato, K. Ishioka, M. Kitajima, J. Tang, R. Saito, and H. Petek, Nano Lett. **8**, 3102 (2008).
[15] J.-H. Kim, K.-J. Han, N.-J. Kim, K.-J. Yee, Y.-S. Lim, G. D. Sanders, C. J. Stanton, L. G. Booshehri, E. H. Hároz, and J. Kono, Phys. Rev. Lett. **102**, 037402 (2009).
[16] C. D. Spataru, S. Ismail-Beigi, L. X. Benedict, and S. G. Louie, Phys. Rev. Lett. **92**, 077402 (2004).
[17] V. N. Popov, New J. Phys. **6**, 17 (2004).
[18] J. Jiang, R. Saito, A. Gruneis, S. G. Chou, G. G. Samsonidze, A. Jorio, G. Dresselhaus, and M. S. Dresselhaus, Phys. Rev. B **71**, 205420 (2005).
[19] M. Machón, S. Reich, H. Telg, J. Maultzsch, P. Ordejón, and C. Thomsen, Phys. Rev. B **71**, 035416 (2005).
[20] F. Valencia, A. H. Romero, H. O. Jeschke, and M. E. Garcia, Phys. Rev. B **74**, 075409 (2006).
[21] M. E. Garcia, T. Dumitrică, and H. O. Jeschke, Appl. Phys. A: Mater. Sci. Process. **79**, 855 (2004).
[22] T. Dumitrica, M. E. Garcia, H. O. Jeschke, and B. I. Yakobson, Phys. Rev. Lett. **92**, 117401 (2004).
[23] T. Dumitrica, M. E. Garcia, H. O. Jeschke, and B. I. Yakobson, Phys. Rev. B **74**, 193406 (2006).
[24] A. Romero, M. Garcia, F. Valencia, H. Terrones, M. Terrones, and H. Jeschke, Nano Lett. **5**, 1361 (2005).
[25] A. Stone and D. Wales, Chem. Phys. Lett. **128**, 501 (1986).
[26] H. O. Jeschke, A. H. Romero, M. E. Garcia, and A. Rubio, Phys. Rev. B **75**, 125412 (2007).
[27] A. M. Weiner and D. E. Leaird, Opt. Lett. **15**, 51 (1990).
[28] A. V. Kuznetsov and C. J. Stanton, Phys. Rev. Lett. **73**, 3243 (1994).
[29] D. Porezag, T. Frauenheim, T. Köhler, G. Seifert, and R. Kaschner, Phys. Rev. B **51**, 12947 (1995).
[30] R. Saito, K. Sato, Y. Oyama, J. Jiang, G. G. Samsonidze, G. Dresselhaus, and M. S. Dresselhaus, Phys. Rev. B **72**, 153413 (2005).
[31] J. W. Jiang, H. Tang, B. S. Wang, and Z. B. Su, Phys. Rev. B **73**, 235434 (2006).
[32] C. Lobo and J. L. Martins, Z. Phys. D: At., Mol. Clusters **39**, 159 (1997).
[33] O. Madelung, *Introduction to Solid-State Theory* (Springer-Verlag, Berlin, 1978).
[34] G. D. Mahan and G. S. Jeon, Phys. Rev. B **70**, 075405 (2004).
[35] R. A. Jishi, L. Venkataraman, M. S. Dresselhaus, and G. Dresselhaus, Chem. Phys. Lett. **209**, 77 (1993).
[36] K. I. Sasaki, R. Saito, G. Dresselhaus, M. S. Dresselhaus, H. Farhat, and J. Kong, Phys. Rev. B **78**, 235405 (2008).
[37] K. I. Sasaki, R. Saito, G. Dresselhaus, M. S. Dresselhaus, H. Farhat, and J. Kong, Phys. Rev. B **77**, 245441 (2008).
[38] J. Jiang, R. Saito, A. Grüneis, G. Dresselhaus, and M. Dresselhaus, Chem. Phys. Lett. **392**, 383 (2004).
[39] H. Ajiki and T. Ando, Physica B **201**, 349 (1994).
[40] V. N. Popov and L. Henrard, Phys. Rev. B **70**, 115407 (2004).
[41] A. Gruneis, R. Saito, G. G. Samsonidze, T. Kimura, M. A. Pimenta, A. Jorio, A. G. Souza Filho, G. Dresselhaus, and M. S. Dresselhaus, Phys. Rev. B **67**, 165402 (2003).
[42] S. L. Chuang, *Physics of Optoelectronic Devices* (Wiley, New York, 1995).
[43] G. D. Sanders, C. J. Stanton, and C. S. Kim, Phys. Rev. B **64**, 235316 (2001).
[44] G. D. Sanders and C. J. Stanton, Phys. Rev. B **74**, 205303 (2006).
[45] R. Liu, G. D. Sanders, C. J. Stanton, C. S. Kim, J. S. Yahng, Y. D. Jho, K. J. Yee, E. Oh, and D. S. Kim, Phys. Rev. B **72**, 195335 (2005).
[46] G.-W. Chern, C.-K. Sun, G. D. Sanders, and C. J. Stanton, in *Topics in Applied Physics*, edited by K.-T. Tsen (Springer-Verlag, New York, 2004), Vol. 92, pp. 339–394.
[47] F. Bassani and G. P. Parravicini, *Electronic States and Optical Transitions in Solids* (Pergamon, New York, 1975).
[48] W. H. Press, S. A. Teukolsky, W. T. Vetterling, and B. P. Flannery, *Numerical Recipes* (Cambridge University Press, New York, 1992).
[49] J. Jiang, R. Saito, A. Grüneis, G. Dresselhaus, and M. Dresselhaus, Carbon **42**, 3169 (2004).
[50] R. Saito, A. Jorio, J. H. Hafner, C. M. Lieber, M. Hunter, T. McClure, G. Dresselhaus, and M. S. Dresselhaus, Phys. Rev. B **64**, 085312 (2001).
[51] T. Ando, J. Phys. Soc. Jpn. **74**, 777 (2005).
[52] M. Dresselhaus, G. Dresselhaus, R. Saito, and A. Jorio, Annu. Rev. Phys. Chem. **58**, 719 (2007).
[53] T. Ando, J. Phys. Soc. Jpn. **66**, 1066 (1997).
[54] R. B. Capaz, C. D. Spataru, S. Ismail-Beigi, and S. G. Louie, Phys. Rev. B **74**, 121401(R) (2006).
[55] G. Dukovic, F. Wang, D. Song, M. Y. Sfeir, T. F. Heinz, and L. E. Brus, Nano Lett. **5**, 2314 (2005).
[56] Y. Miyauchi, R. Saito, K. Sato, Y. Ohno, S. Iwasaki, T. Mizutani, J. Jiang, and S. Maruyama, Chem. Phys. Lett. **442**, 394 (2007).
[57] Z. M. Li, V. N. Popov, and Z. K. Tang, Solid State Commun. **130**, 657 (2004).
[58] V. N. Popov, V. E. Van Doren, and M. Balkanski, Phys. Rev. B **59**, 8355 (1999).
[59] A. Grüneis, Ph.D. thesis, Tohoku University, Sendai, Japan, 2004.